Aeolian Research 30 (2018) 97–114

Contents lists available at ScienceDirect

Aeolian Research

journal homepage: www.elsevier.com/locate/aeolia

High-frequency measurements of aeolian saltation flux: Field-based methodology and applications

Raleigh L. Martin[a,*], Jasper F. Kok[a], Chris H. Hugenholtz[b], Thomas E. Barchyn[b], Marcelo Chamecki[a], Jean T. Ellis[c]

[a] Department of Atmospheric and Oceanic Sciences, University of California, Los Angeles, CA 90095, USA
[b] Department of Geography, University of Calgary, Calgary, AB, Canada
[c] Department of Geography and School of Earth, Ocean and Environment, University of South Carolina, Columbia, SC 29208, USA

ARTICLE INFO

Keywords:
Aeolian transport
Saltation
Wind erosion
Turbulence
Boundary layer processes
Field-based measurements

ABSTRACT

Aeolian transport of sand and dust is driven by turbulent winds that fluctuate over a broad range of temporal and spatial scales. However, commonly used aeolian transport models do not explicitly account for such fluctuations, likely contributing to substantial discrepancies between models and measurements. Underlying this problem is the absence of accurate sand flux measurements at the short time scales at which wind speed fluctuates. Here, we draw on extensive field measurements of aeolian saltation to develop a methodology for generating high-frequency (up to 25 Hz) time series of total (vertically-integrated) saltation flux, namely by calibrating high-frequency (HF) particle counts to low-frequency (LF) flux measurements. The methodology follows four steps: (1) fit exponential curves to vertical profiles of saltation flux from LF saltation traps, (2) determine empirical calibration factors through comparison of LF exponential fits to HF number counts over concurrent time intervals, (3) apply these calibration factors to subsamples of the saltation count time series to obtain HF height-specific saltation fluxes, and (4) aggregate the calibrated HF height-specific saltation fluxes into estimates of total saltation fluxes. When coupled to high-frequency measurements of wind velocity, this methodology offers new opportunities for understanding how aeolian saltation dynamics respond to variability in driving winds over time scales from tens of milliseconds to days.

1. Introduction

Wind-blown (aeolian) transport of sand shapes a variety of desert, coastal, and planetary landscapes (e.g., Lancaster, 1988; Bridges et al., 2012; Durán and Moore, 2013). Saltation, the ballistic hopping motion of wind-blown sand grains, drives the bulk of aeolian sand flux (Bagnold, 1941), abrades bedrock (Perkins et al., 2015), erodes soil (Chepil, 1945), and generates airborne dust through impacts with the soil surface (Gillette et al., 1974; Shao et al., 1993; Marticorena and Bergametti, 1995; Kok et al., 2014). Studies of landscape evolution and dust generation require models that accurately relate wind speed, surface conditions, and the resulting sand flux (e.g., Kok et al., 2012).

Unfortunately, aeolian saltation models often do a poor job of predicting rates of sand transport in natural environments (e.g., Kok et al., 2012; Sherman and Li, 2012; Sherman et al., 2013; Barchyn et al., 2014b). Most existing aeolian saltation models are based on the assumption of a steady-state momentum balance (e.g., Ungar and Haff, 1987; Andreotti, 2004), but saltation in natural environments is driven by widely-varying turbulence spectra, which produce broad spatial and temporal variations in the saltation flux (e.g., Baas, 2006; Durán et al., 2011). Though wind-tunnel experiments can capture some of this turbulent variability (e.g., Li and McKenna Neuman, 2012, 2014), such experimental settings differ substantially from natural environments in their ability to capture saltation-wind interactions (e.g., Sherman and Farrell, 2008), producing broad unexplained discrepancies between field and laboratory measurements (Barchyn et al., 2014b; Martin and Kok, 2017a). In addition, sedimentological factors like soil moisture (Arens, 1996; Davidson-Arnott et al., 2008), surface crusting (Gillette et al., 1982), sediment availability (Webb et al., 2016a), electrification (e.g., Kok and Renno, 2008), mid-air particle collisions (e.g., Sørensen and McEwan, 1996; Carneiro et al., 2013), and surface grain-size distributions (Iversen and Rasmussen, 1999), cause further differences among models, wind tunnel experiments, and field measurements. Though recent studies have sought to understand each individual factor governing aeolian saltation dynamics separately, our ability to model how this constellation of atmospheric and sedimentological factors

* Corresponding author.
E-mail address: raleighmartin@gmail.com (R.L. Martin).

https://doi.org/10.1016/j.aeolia.2017.12.003
Received 19 June 2017; Received in revised form 18 December 2017; Accepted 18 December 2017

interact to control the aeolian saltation flux remains limited. Coupled high-frequency (HF) field measurements of wind and saltation offer the potential to improve our understanding of some of the atmospheric factors affecting saltation flux variability, and they can also help to constrain the role of sedimentological factors (e.g., Martin and Kok, 2017a).

Until recently, field-based observations of aeolian saltation have been limited to low-frequency (LF) measurements with saltation traps (i.e., sampling interval $\geqslant \sim 1$ min. These traps generally provide reliable measures of the saltation mass flux over time scales of minutes to days (e.g., Greeley et al., 1996; Sherman et al., 1998; Namikas, 2003), though comparative studies reveal variations in trap accuracy that depend on wind speed and airborne grain sizes (e.g., Goossens et al., 2000). Assuming that saltation traps do indeed provide reliable measures of the saltation flux, LF studies are useful for relating saltation flux and vertical saltation profile characteristics (Greeley et al., 1996; Namikas, 2003; Farrell et al., 2012) to time-averaged wind speeds (Sherman et al., 1998; Sherman and Li, 2012). However, such LF studies are unable to resolve the HF spatial and temporal variability in saltation flux (i.e., $\leqslant \sim 1$ min) resulting from wind turbulence in the atmospheric boundary layer (e.g., Baas and Sherman, 2005). Such variability is thought to produce much of the disagreement between measurements and models of aeolian saltation flux (Barchyn et al., 2014b).

To better resolve turbulence-induced saltation fluctuations, a variety of new HF sensors have been deployed in field studies over the past two decades (e.g., Baas, 2004; Barchyn and Hugenholtz, 2010; Sherman et al., 2011). HF measurements typically register individual sand grains, using sensors with optical gates (e.g., Hugenholtz and Barchyn, 2011; Etyemezian et al., 2017), piezoelectric impact plates (e.g., Barchyn and Hugenholtz, 2010; Sherman et al., 2011), or acoustic microphones (e.g., Spaan and van den Abeele, 1991; Ellis et al., 2009b). Such sensors are capable of recording measurements at time scales ranging from tens of milliseconds to seconds (e.g., Sterk et al., 1998; Baas, 2008; Martin et al., 2013), much faster than the most rapid automated saltation trap sampling techniques (Bauer and Namikas, 1998; Butterfield, 1991; Namikas, 2002; Ridge et al., 2011).

HF saltation sensors have been used in recent years to address a variety of questions in aeolian research. Recent field studies deploying HF saltation sensors, in tandem with HF anemometer wind observations, have quantified the frequently observed spatial and temporal patterns of alternating high and low saltation flux known as “aeolian streamers” (Baas and Sherman, 2005; Weaver and Wiggs, 2011). Other HF field deployments have offered further insight on the temporal variability of saltation flux (Sterk et al., 1998; Schonfeldt and von Lowis, 2003; Baas, 2006; Martin et al., 2013), across complex topography (Bauer et al., 2015, 2012; Davidson-Arnott et al., 2012; Hoonhout and de Vries, 2017) and around vegetation (Barrineau and Ellis, 2013; Chapman et al., 2013). HF sensors are also vital for describing saltation intermittency and thresholds (Stout and Zobeck, 1997; Schönfeldt, 2004; Wiggs et al., 2004a; Barchyn and Hugenholtz, 2011; Poortinga et al., 2015; Webb et al., 2016a) and the effects of humidity and soil moisture on these thresholds (Arens, 1996; Wiggs et al., 2004b; Delgado-Fernandez et al., 2012). Optical HF sensors have also been used extensively for the measurement of wind-driven snow transport (Leonard et al., 2011; Bellot et al., 2013; Maggioni et al., 2013; Trujillo et al., 2016).

Though helpful for advancing the understanding of saltation dynamics, HF measurements typically provide only relative, not absolute, measures of the aeolian saltation flux (e.g., Barchyn et al., 2014a). Typically, these HF sensors produce data in counts per second. Such count rates are only internally relative and require a conversion to physically meaningful quantities, which may not be as simple as one grain per count (Barchyn et al., 2014a). For certain research purposes, these relative HF saltation measurements are sufficient, such as for studies of saltation intermittency and thresholds at a single point (e.g., Stout and Zobeck, 1997; Martin and Kok, 2017b). However, to understand the relationship between turbulence structures and saltation flux variability in space and time, absolute HF measurements of saltation flux are needed (e.g., Martin et al., 2013; Bauer et al., 2015; Hoonhout and de Vries, 2017).

To address the need for reliable HF saltation flux measurements, studies have compared the performance of different HF sensors (e.g., Davidson-Arnott et al., 2009; Leonard et al., 2011; Massey, 2013) and assessed the comparability of HF particle counts to LF trap saltation fluxes (e.g., Sterk et al., 1998; Goossens et al., 2000; Sherman et al., 2011). Though these studies generally reveal linear relationships among particle counts from different sensors (e.g., Barchyn et al., 2014a), they also indicate substantial differences in sensitivity between sensors of the same type (Baas, 2008) or among sensors of different types (Hugenholtz and Barchyn, 2011). HF saltation sensors are potentially subject to “saturation” effects – i.e., reaching a maximum saltation flux above which measured particle counts no longer increase (Hugenholtz and Barchyn, 2011; Sherman et al., 2011). HF sensors may also have response sensitivities to momentum or particle size (Barchyn et al., 2014a). Additionally, HF sensors may display “drift”, or variation in their performance through time, due to environmental conditions causing sensor degradation (Hugenholtz and Barchyn, 2011; Bauer et al., 2012; Barchyn et al., 2014a).

A fundamental issue with most HF measurements is that, whereas traps and sensors typically provide only height-specific values for the saltation flux, models of aeolian saltation consider total (vertically-integrated) saltation fluxes (e.g., Bagnold, 1941; Owen, 1964; Ungar and Haff, 1987; Andreotti, 2004). To facilitate direct comparisons of these height-specific saltation measurements to the total vertically-integrated saltation fluxes considered in numerical (e.g., Dupont et al., 2013), analytical (e.g., Pähtz et al., 2013), and wind-tunnel (e.g., Li and McKenna Neuman, 2014) studies of HF saltation variability, measurements from sensors at multiple heights must be combined to provide estimates of the total saltation flux. Turbulent variability and counting uncertainties may hinder the convergence of these profiles to expected exponential (Ellis et al., 2009a; Fryrear and Saleh, 1993; Namikas, 2003; Dong et al., 2012) or other (Zobeck and Fryrear, 1986; Dong et al., 2011) profile shapes over short time scales (e.g., Bauer and Davidson-Arnott, 2014). Thus, existing studies of high-frequency saltation flux variability are limited to examination of relative or height-specific saltation fluxes (e.g., Baas, 2008).

In short, LF trap and HF sensor measurement techniques each have distinctive advantages and disadvantages for determining saltation flux. LF measurements can accurately measure horizontal and vertical profiles of mass flux and sediment size, but they can detect only the broadest fluctuations of saltation mass flux associated with the passage of large-scale turbulent structures (McKenna Neuman et al., 2000). HF sensors can resolve saltation responses to turbulence, but their ability to provide absolute mass fluxes is questionable (Hugenholtz and Barchyn, 2011). Ideally, the respective advantages of LF and HF measurements could be combined to provide HF time series of absolute saltation flux.

In this paper, we describe a new methodology to generate reliable high-resolution time series of the total (vertically-integrated) saltation mass flux. Specifically, we do so by using absolute LF measurements from sediment traps to calibrate relative HF measurements from optical particle counters. Though such calibration has been performed in the past (e.g., Martin et al., 2013; Haustein et al., 2015), we provide here a much more systematic development, testing, and explanation for a calibration-based methodology to obtain HF time series of vertical saltation profiles and total saltation fluxes. To do so, we first describe the three field sites at which we collected LF and HF saltation measurements (Section 2) and the instrumentation involved in these measurements (Section 3). In Section 4 we describe the sequence of steps for obtaining calibrated, high-frequency measurements of the total saltation flux, and we present some illustrative results. In the Discussion (Section 5), we outline the advances and limitations of the HF saltation

calibration methodology, and we offer guidelines for future field deployments. We conclude and summarize our findings in Section 6.

2. Field sites

In this section, we provide basic information about the three field sites for our data collection and the grain-size characteristics of the surface sediments at these sites.

2.1. General information about field sites

We measured aeolian saltation at three sites: Jericoacoara, Ceará, Brazil (2.7969°S, 40.4837°W); Rancho Guadalupe, California, United States (34.9592°N, 120.6431°W); and Oceano, California, United States (35.0287°N, 120.6277°W). The Jericoacoara site is located on a gently undulating sand sheet approximately 250 m downwind of a patch of gravel and vegetation and 750 m from the Atlantic Ocean shoreline under dominantly easterly sea breezes. The Rancho Guadalupe site is located on a flat sand patch approximately 100 m from a canyon containing the Santa Maria River estuary and 950 m from the Pacific Ocean shoreline. The Oceano site is located on a gently sloped (up in landward direction) sand patch approximately 300 m downwind of coastal foredunes and 650 m from the Pacific Ocean shoreline. Both the Rancho Guadalupe and Oceano sites, separated by about 10 km, are contained within the Guadalupe-Nipomo Dune Complex (Cooper, 1967) shaped by dominantly westerly sea breezes. Additional information is provided in Table 1.

2.2. Grain-size distributions

We analyzed grain-size distributions of sand samples collected from the bed surface and from airborne sand traps at each field site. For all of these samples, we obtained particle size distributions by volume using a Retsch Camsizer optical grain size analysis instrument, located at the Sediment Dynamics Laboratory at the University of Pennsylvania (Jerolmack et al., 2011).

To collect the samples, we used a trowel to scrape up the top ~1 cm of surface sand at the beginning and end of each field day. To discern the "typical" grain size distribution from the samples, we averaged all surface grain size distributions into a single representative distribution (Fig. 1). We estimated 10th, 50th, and 90th percentile index values – d_{10}, d_{50}, and d_{90}, respectively – for each site-averaged grain-size distribution (Table 1). We estimated the corresponding uncertainties in these site-averaged index values as the standard deviation of grain-size index values for individual samples.

We also collected airborne samples in BSNE (Big Springs Number Eight) sand traps (Fryrear, 1986) deployed at various heights above the sand surface. We found no systematic variation of grain size with shear velocity, but we did notice changes in grain size with height above the sand surface. In Section 4.2.3 we consider the effect of vertical variations in the airborne grain size with height to interpret some of the variability in the calibration factors used to convert from relative to absolute saltation fluxes for HF sensors.

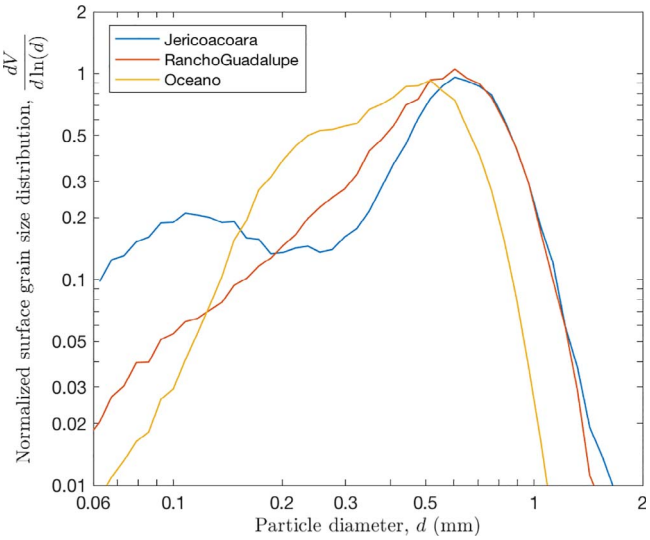

Fig. 1. Grain size distributions determined from surface samples collected at field sites. V is particle volume and d is particle diameter. Jericoacoara and Rancho Guadalupe share a similar 0.6 mm primary modal grain size but differ in their distribution of fine particle sizes (bimodal at Jericoacoara versus unimodal at Rancho Guadalupe). Oceano surface sand is slightly finer (0.5 mm modal grain size) than at the other two sites.

3. Instrumentation

In this section, we describe the instruments used for characterizing wind and saltation and the associated spatial configurations of these instruments (Table 1). As a convention for describing instrument locations, x is the streamwise coordinate (positive downwind), y is the spanwise coordinate (positive according to right-hand rule, i.e., to the right if looking upwind), and z is the vertical coordinate (positive away from the ground surface). We set the origin (x,y,z = 0,0,0) as the sand surface in the center of the HF instrument stand at each site. The x,y coordinate grid remained fixed for each deployment site, while the $z = 0$ level varied through time with sand aggradation and deflation at each site, as we explain further below.

3.1. Wind measurements

Sonic anemometers (RM Young 81000 recording at 25 Hz at Jericoacoara and Rancho Guadalupe and Campbell CSAT3 recording at 50 Hz at Oceano) made high-frequency measurements of the three-

Table 1
Summary information for field sites.

	Jericoacoara	Rancho Guadalupe	Oceano
Coordinates	2.7969°S, 40.4837°W	34.9592°N, 120.6431°W	35.0287°N, 120.6277°W
Deployment dates	2014-11-13 to 2014-11-20	2015-03-23 to 2015-03-24	2015-05-15 to 2015-06-04
Distance to shoreline (m)	750	950	650
Sand patch distance (m)	250	100	300
Anemometer heights, z_U (m)	*2014-11-13:* 0.48, 0.97, 1.93, 3.02 *2014-11-14:* 0.47, 0.98, 1.76, 2.59 *2015-11-20:* 0.47, 0.97, 1.76, 2.58	*2015-03-23:* 0.45, 1.00, 1.80, 2.75 *2015-03-24:* 0.43, 1.00, 1.79, 2.81	*All dates:* 0.64, 1.16, 2.07, 3.05, 6.00, 8.95
LF trap (BSNE) heights, $z_{LF,i}$ (m)	0.10–0.52	0.08–0.70	0.05–0.46
HF sensor (Wenglor) heights, $z_{HF,i}$ (m)	0.02–0.29	0.02–0.32	0.06–0.47
10th percentile grain diameter, d_{10} (mm)	0.097 ± 0.012	0.219 ± 0.035	0.190 ± 0.032
Median grain diameter, d_{50} (mm)	0.526 ± 0.037	0.533 ± 0.026	0.398 ± 0.070
90th percentile grain diameter, d_{90} (mm)	0.847 ± 0.037	0.839 ± 0.034	0.650 ± 0.075
Active saltation days	3	2	12

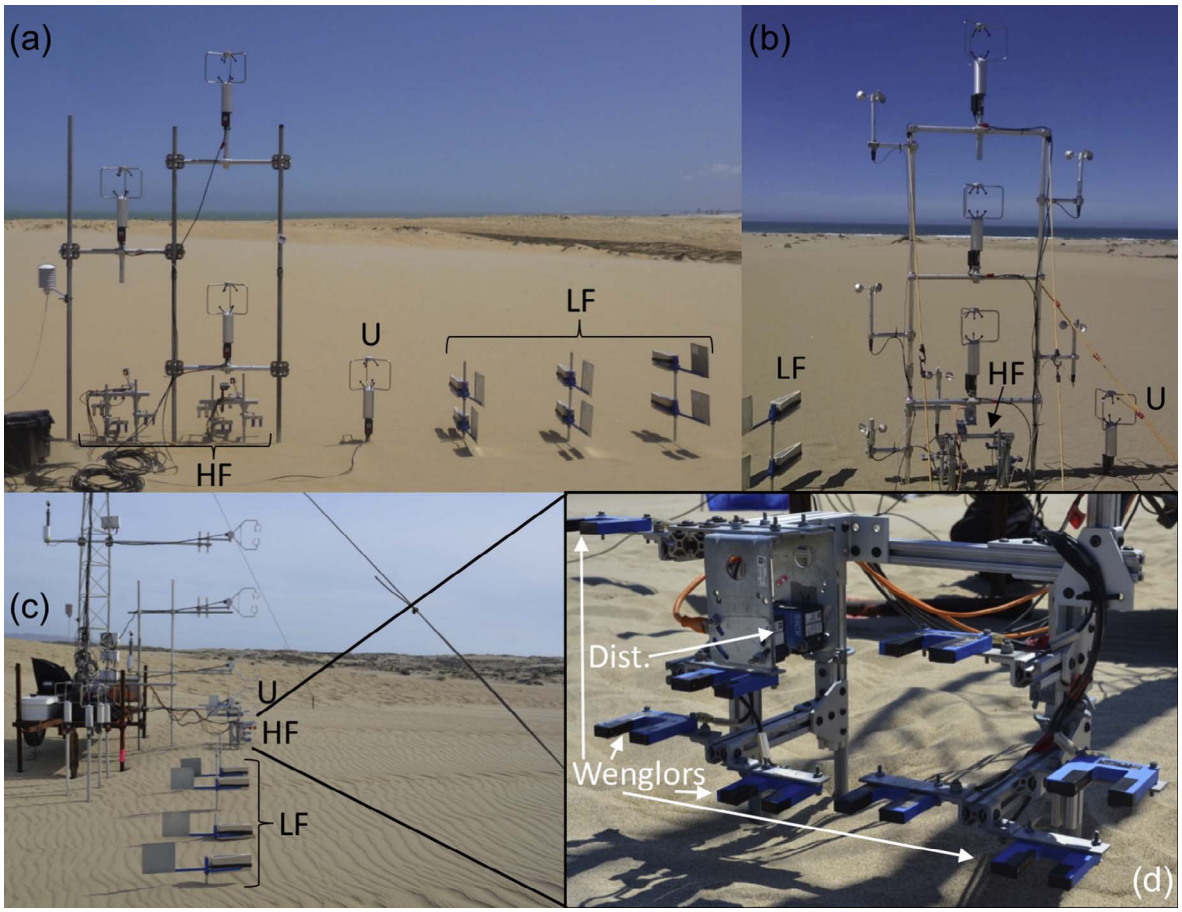

Fig. 2. Photos of field sites, with locations of LF saltation traps, HF saltation sensors, and sonic anemometers indicated for reference. At each site, only the lowermost sonic anemometer (denoted "U") is included in the analysis. (a) Jericoacoara, looking upwind. LF traps were separated into 3 towers, and HF sensors were divided into 2 arrays. (b) Rancho Guadalupe, looking upwind. Some LF traps are not shown in the figure. All HF sensors were included in a single array. (c) Oceano, looking from the side, with + y LF traps in foreground and HF sensors in the background. (d) Close-up of Wenglor and distance sensor array for HF measurements at Oceano, looking downwind.

dimensional wind vector: u,v,w, respectively in the streamwise, spanwise, and vertical directions (x,y,z). Sonic anemometers also collected simultaneous measurements of equivalent temperature, useful for calculations of atmospheric stability. Though we deployed sonic anemometers at multiple heights (Table 1), we used observations only from the lowest sonic anemometer at each site for the analyses described in this paper. These lowermost anemometers were positioned at a height $z_U \approx 0.5$ m above the ground surface (Table 1). We selected the lowest anemometers as most representative of shear stress at the bed and least likely to be affected by boundary layer instability farther from the surface. In support of this choice to use data only from the lowest anemometers, measurements from anemometers higher above the surface yield wind shear stresses similar to those measured by the lowest anemometer (Martin and Kok, 2017a).

3.2. Saltation flux measurements

We used multiple instruments to characterize sand flux. BSNE sand traps at multiple heights above the surface provided absolute LF measurements of saltation flux, but with low time resolution. Wenglor optical particle counters provided HF relative time series of saltation counts, but required calibration to determine absolute fluxes. Downward-facing laser distance sensors measured local bed elevation to determine changes in saltation sensor heights through time, thus aiding the HF saltation flux calibration procedure (Supporting Information Fig. S1).

In our subsequent descriptions, we use the subscript "LF" to specify low-frequency measurements and calculations from the BSNEs, and the subscript "HF" to specify high-frequency measurements from the Wenglors. We adopt these subscripts with the understanding that such measurements and calculations could also be made for other types of LF traps and HF sensors.

3.2.1. BSNE sand traps for low-frequency (LF) measurements

BSNE sand traps (Fryrear, 1986) collected airborne saltating sand over fixed time intervals at multiple heights. BSNEs are well calibrated and provide high collection efficiency (Goossens et al., 2000); however, as we further discuss in Section 5.2.1, BSNEs also present limitations in their bulkiness and the resulting need to mount them high above the bed surface for extended periods of time. Most of the BSNEs were the standard type, with vertical opening size $H_{LF} = 5$ cm and horizontal opening size $W_{LF} = 2$ cm. The one exception was one 'modified' BSNE with $H_{LF} = 1$ cm, which we deployed at the Oceano site to measure saltation flux close to the surface.

BSNEs were attached to wind vanes on vertical poles, allowing them to rotate freely with the prevailing wind direction. We placed all BSNEs at the same streamwise position, $x = 0$, corresponding with all other instruments. To increase the vertical (z) resolution of the BSNE profile, we placed BSNEs at multiple spanwise (y) locations, because trap bulkiness made close vertical spacing of all BSNEs at the same y position impossible. At the beginning and end of each field day, we measured the vertical distance from the ground to the bottom of the trap opening $z_{bot,LF,i}$ for each trap i.

We performed BSNE trap collections for specified time intervals T_{LF}, usually one hour. Occasionally, we modified T_{LF} to ensure that traps collected a reasonable amount of sand: we extended T_{LF} during periods

of very weak saltation and shortened T_{LF} during periods of intense saltation. We weighed all BSNE samples in the lab using a SmartWeigh Pro Pocket Scale TOP2KG (accuracy ± 0.1 g) to determine saltation masses $m_{LF,i}$ for each BSNE and each time interval.

3.2.2. Wenglor optical particle counters for high-frequency (HF) measurements

Wenglor optical particle counters (model YH03PCT8 with 3 cm path length) detected passage of individual saltators at multiple heights $z_{HF,i}$ above the bed surface. Wenglor sensors then transmitted these detections as pulses to a Campbell CR1000 datalogger recording at 25 Hz, thus providing HF measurements of saltation pulse counts n_i for each sensor i. Due to frequent blockage of Wenglor lenses by dust, which manifested as abrupt unexplained changes in the n_i time series, we often excluded specific sensors from our analyses. The number of HF sensors included in analyses therefore varied from 3 to 9. Time intervals with fewer than 3 Wenglors were excluded as insufficient for fitting saltation flux profiles.

3.2.3. Laser distance sensors for bed elevation

Laser distance sensors (Sick DT35), co-located with the Wenglor laser particle counters, were pointed downward toward the surface to measure changes of bed elevation through time. Based on these distances and known relative vertical distances between each Wenglor i and distance sensors, we estimated absolute elevations for each Wenglor $z_{HF,i}$.

3.3. Instrument layouts

Instrument layouts varied from site to site, as illustrated in Fig. 2. We detail the layouts of specific instrument types below.

At all field sites, measurements from the sonic anemometer, BSNE traps, and Wenglor sensors were co-located in the streamwise direction at $x = 0$. In the spanwise (y) direction, we positioned the BSNE traps away from the Wenglors and sonic anemometer to reduce interference among instruments. At Jericoacoara, we placed all BSNEs on one side ($+y$) of the Wenglors and anemometer (Fig. 2a). At Rancho Guadalupe and Oceano, we placed BSNEs on both sides of the setup ($\pm y$) (Fig. 2b), though BSNEs were more widely spaced at Oceano ($y \approx \pm 5$ m) (Fig. 2c). At Jericoacoara and Rancho Guadalupe, Wenglors were also separated in the y-direction from sonic anemometers (Fig. 2a and b), whereas the sonic anemometer and Wenglors shared the same $y \approx 0$ at Oceano (Fig. 2c).

In addition to the spanwise separation of different measurements types, we separated individual BSNE traps in the y-direction to accommodate the vertical size of individual traps (each standard BSNE's total height is ~7 cm). We also separated individual Wenglor sensors to reduce airflow interference and particle ricochets among sensors, which we found to be problematic when deploying Wenglors as a single vertical stack. The maximum spanwise BSNE separations were 1.5 m, 3 m, and 10 m at Jericoacoara, Rancho Guadalupe, and Oceano, respectively. We adopted a much wider BSNE spanwise separation at Oceano to reduce potential instrument interference issues at this site. The maximum spanwise Wenglor separations were 1.2 m, 0.6 m, and 0.6 m at Jericoacoara, Rancho Guadalupe, and Oceano, respectively. We discuss the possible effects of spanwise trap and sensor separation in Section 5.1.2.

For practical reasons, all Wenglors and laser distance sensors were mounted onto fixed stands, unable to rotate with the wind like the BSNE traps. As wind direction during saltation varied within a narrow range of ± 15° (Martin and Kok, 2017a), we expect that the combination of rotating LF traps and rigid HF sensors had only a small effect on our analyses, and that these variations were likely captured in the calibration factors. Nonetheless, it is possible that shifts in wind direction producing misalignment between rotating BSNEs and rigidly mounted Wenglors could have caused changes in HF sensor particle count rates with respect to LF collected saltation fluxes, such as through changes in the projected length of the Wenglor laser beam or in the effects of the sensor on the local wind field. In Section 4.2.3 below, we further consider the uncertainty introduced by the combination of rotating LF traps and fixed HF sensors used in our study.

For practical reasons, the configurations of HF sensors varied among field sites. At Jericoacoara, we mounted Wenglors in a vertical orientation with prongs facing downward, and these Wenglors were mounted on two separate stands (Fig. 2a). At Rancho Guadalupe and Oceano, we mounted Wenglors horizontally with prongs facing upwind, and these Wenglors were mounted on a single stand (Fig. 2b–d). We mounted distance sensors at known heights $z_{rel,i}$ relative to HF sensors directly on each Wenglor stand, providing height reference for all HF measurements. Fig. 2d provides a close-up view of the Wenglor and distance sensor mounting at Oceano.

4. Methodology and illustrative results

In this section, we explain the four-step methodology for obtaining calibrated, high-resolution measurements of the total (vertically-integrated) saltation flux. The sequence of steps is as follows: (1) perform exponential fits to LF trap vertical profiles of saltation flux, (2) determine the empirical calibration factors through comparison of LF exponential fits to HF number counts over concurrent time intervals, (3) apply these calibration factors to subsamples of the saltation count time series to obtain HF height-specific saltation fluxes, and (4) aggregate the calibrated HF height-specific saltation fluxes into total saltation fluxes through application of profile fitting and summation techniques. An overview of these methods is shown in Fig. 3. In addition, we provide a glossary of all variables used to describe this methodology in Supporting Information Section S2.

4.1. Calculating and fitting low-frequency (LF) saltation flux profiles from BSNE traps

Here, we describe methods for computing height specific saltation fluxes from LF traps (Section 4.1.1) and performing exponential fits to these profiles (Section 4.1.2). Though we describe these calculations specifically for measurements from BSNE traps, this methodology is meant to be applicable to all vertical profiles of LF saltation measurements, regardless of trap type.

4.1.1. Calculating LF height-specific saltation fluxes

We calculate the LF height-specific horizontal saltation flux $q_{LF,i}$ for the ith trap based on the measurement interval of duration T_{LF} (typically 1 h, see Section 3.2.1), the trap opening height H_{LF}, trap width W_{LF}, and total mass of sand collected $m_{LF,i}$:

$$q_{LF,i} = \frac{m_{LF,i}}{T_{LF} H_{LF} W_{LF}} \tag{1}$$

The parameters describing trap dimensions are illustrated in Fig. 4. We compute flux uncertainty $\sigma_{q_{LF,i}}$ through propagation of the quantities included in the calculation (see Supporting Information Section S1.4).

4.1.2. Exponential fits to LF flux profiles

We perform exponential fits to vertical profiles of $q_{LF,i}$, which take the form:

$$q_{exp,LF,i} = q_{0,LF} \exp\left(-\frac{z_{LF,i}}{z_{q,LF}}\right), \tag{2}$$

where $q_{exp,LF,i}$ is the exponential best-fit saltation flux for trap i, $z_{LF,i}$ is the height of trap i, $q_{0,LF}$ is the best-fit scaling parameter, and $z_{q,LF}$ is the best-fit e-folding saltation layer height for the profile (Supporting Information Fig. S2). (At Oceano, where sets of traps were widely separated in the transverse direction, we compute $q_{0,LF}$ and $z_{q,LF}$ as the mean of fit values from two profiles – see Supporting Information Fig.

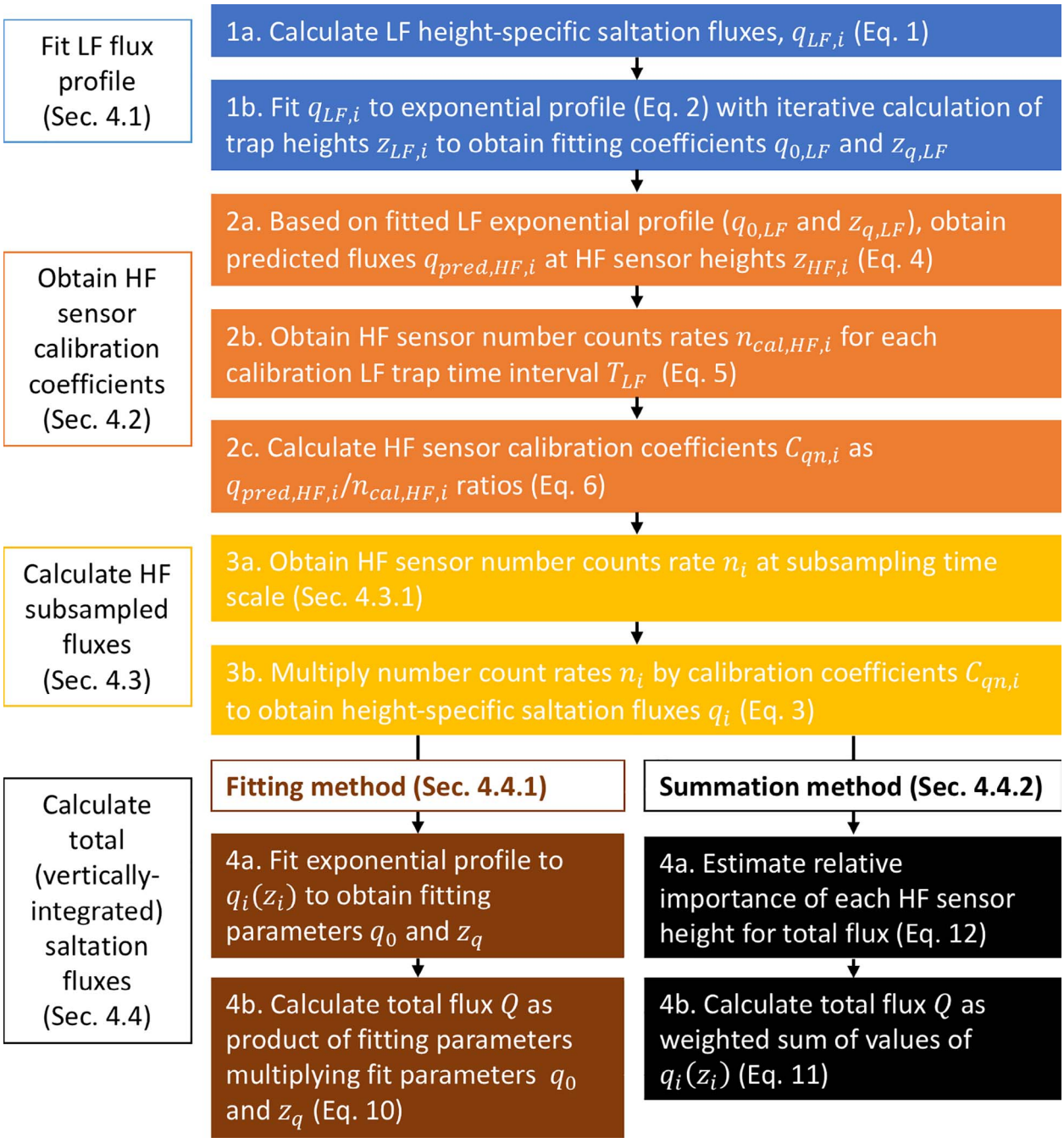

Fig. 3. Flow chart overview of methodology for obtaining the total (vertically-integrated) saltation flux from the LF and HF measurements.

S3.)

Because trap collection of sand spanned a vertical range H_{LF} from the bottom of the trap $z_{bot,LF,i}$ (Fig. 4), we calculate $z_{LF,i}$ as a representative height for each trap. In particular, we perform an iterative calculation to choose the value for $z_{LF,i}$ that optimizes the representation of the exponential flux profile within the trap as a single point value for the entire trap (See Supporting Information Section S1.5). We find such $z_{LF,i}$ values to be mostly statistically indistinguishable from values estimated from the geometric mean height for each trap (Ellis et al., 2009a); however, heights calculated by these methods do diverge close to the bed surface (Supporting Information Fig. S4).

To confirm the appropriateness of the exponential profile fit, we compare the quality of this fit to a power law fit (Supporting Information Section S1.6). We find the exponential fit to consistently perform better than the power law (Supporting Information Fig. S5), thus justifying its use here and henceforth in this analysis.

4.2. Calibrating high-frequency (HF) saltation mass fluxes

In this subsection, we describe methods for obtaining calibration factors $C_{qn,i}$, which can be used to convert HF sensor counts to absolute saltation fluxes, i.e.:

$$q_i = C_{qn,i} n_{HF,i}, \tag{3}$$

where q_i is the calibrated saltation flux and n_i is the HF sensor count rate over a time interval Δt. To determine values for $C_{qn,i}$, we compare absolute mass fluxes obtained from LF flux profiles to HF sensor counts measured over concurrent time intervals (Fig. 5), here collected with Wenglor optical particle counters sampling at 25 Hz.

Below, we describe the steps in this calibration process, then we

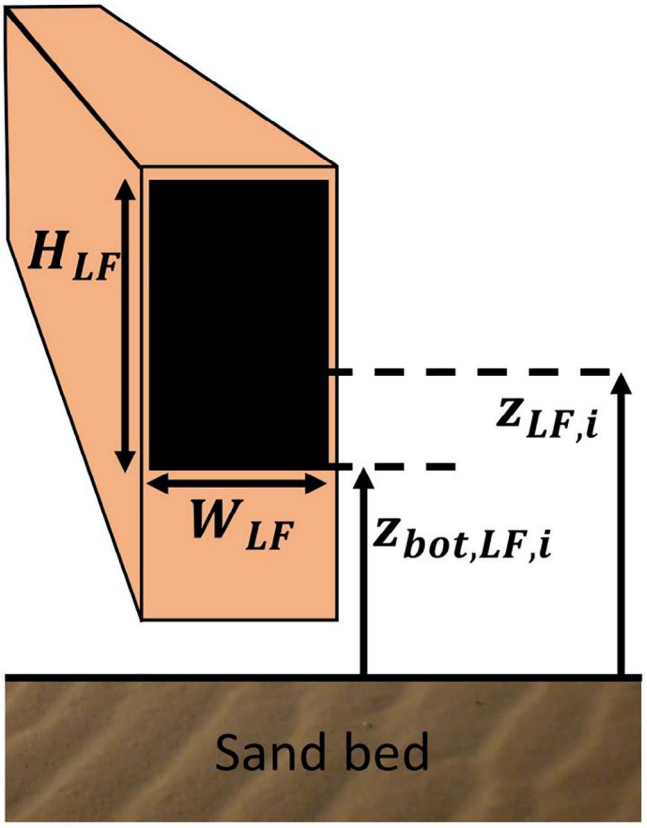

Fig. 4. Illustration of variables describing the geometry of the LF trap opening and positioning for calculations in Section 4.1. H_{LF} is trap opening height, W_{LF} is trap width, $z_{bot,LF,i}$ is the bottom elevation of the trap opening, and $z_{LF,i}$ is the calculated representative height of the trap opening.

evaluate the quality of the resulting calibration factors. Before detailing this calibration process, we first describe our quality control procedures for determining which HF sensors to consider for analysis.

4.2.1. HF sensor quality control

To determine which HF sensors to include in the calibration process for each measurement time interval, we consider two criteria: (1) the height of the sensor above the surface, and (2) the stability of the saltation number counts time series in comparison to other sensors. For the first criterion, we set a lower limit HF sensor height $z_{HF,i} = 1.8$ cm, below which we exclude sensors from analysis. This height represents the minimum distance of the sensor from the ground, such that the bottom of the instrument (in our case, the Wenglor optical particle counter) is separated from the ground by at least one instrument width. Because of the effects of changing bed elevation due to migrating ripples and scour, we found that relative uncertainties of HF sensor heights for $z_{HF,i} < 1.8$ cm were too large for inclusion in the analysis.

To evaluate the second criteria, we compare time series of detected saltation particle counts across all sensors to diagnose drift in sensor performance. Due to differences in sensor heights and sensitivities, we expect substantial differences in long-term mean particle count rates among sensors. However, we also expect that these differences among sensors should remain stable – that each sensor displays roughly corresponding fluctuations in particle counts through time. In cases where one or more sensors displays sudden changes or significant long-term trends not reflected in saltation count time series from other sensors, we consider it likely that the sensor performance was degraded by dust build-up on the lens or other factors causing a slow decline in count rate, or a sudden inability to count particles when the laser is blocked (Hugenholtz and Barchyn, 2011; Barchyn et al., 2014a). Therefore, we exclude such malfunctioning sensors from subsequent calibration and analysis. This quality control protocol is an evolved version of the recommendations of Barchyn et al. (2014a), who suggest that all Wenglor sensors should be deployed in pairs to provide cross-checks on sensor counts.

The HF sensor calibration methods and subsequent flux calculations described below apply only to those sensors that fulfilled our two quality control criteria: high enough off the ground (i.e., $z_{HF,i} > 1.8$ cm) and relatively unaffected by long-term drift or sensor failure.

4.2.2. Obtaining calibration factors

Fig. 5 details the three primary steps in obtaining calibration factors $C_{qn,i}$. First, we extrapolate LF profile exponential fits for each

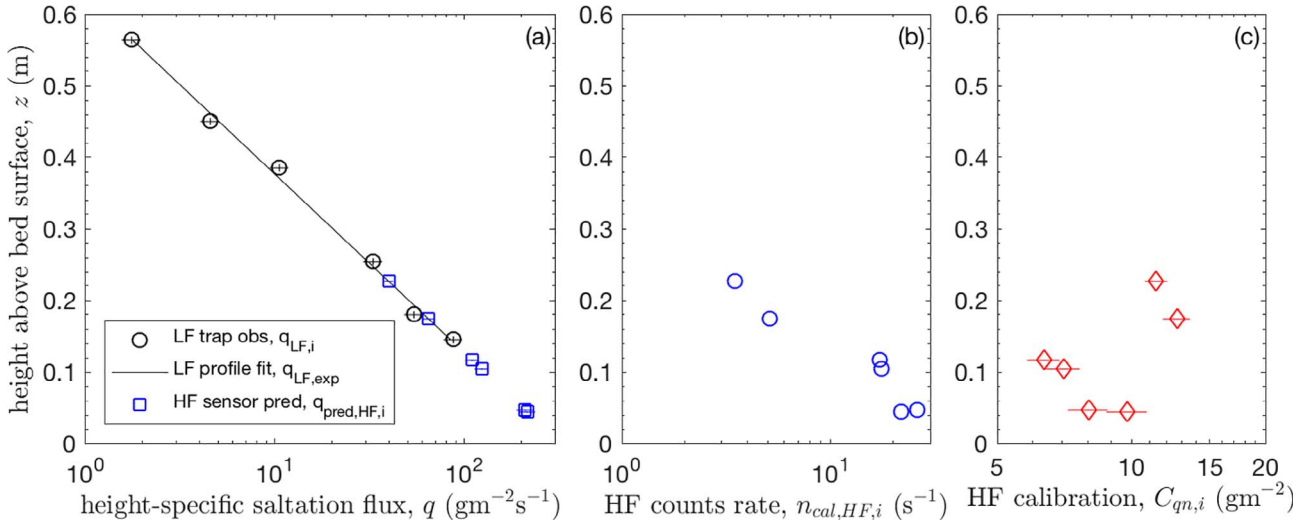

Fig. 5. Demonstration of the three primary steps in the method for determining HF sensor calibration factors, as laid out in detail in Section 4.2 of this paper. The data are from Jericoacoara on 14 November 2014, from 15:26 to 16:26 local time. (a) First, we predict the saltation fluxes at the heights of the HF sensors. To do this, we obtain the exponential fit $q_{exp,LF}$ (Eq. (2) – black line) to LF trap saltation fluxes $q_{LF,i}$ versus trap heights $z_{LF,i}$ (black circles), then we extrapolate from this exponential fit to get expected saltation fluxes at HF sensor heights $q_{pred,HF,i}$ (Eq. (4) – blue squares). (b) Second, we obtain the corresponding HF sensor number count rate over the calibration interval $n_{cal,HF,i}$ (Eq. (5) – blue circles). (c) Third, we compute the ratio of $q_{pred,HF,i}$ (panel a) and $n_{cal,HF,i}$ (panel b) to obtain the calibration factors for HF sensors $C_{qn,i}$ (Eq. (6) – red diamonds). (For interpretation of the references to colour in this figure legend, the reader is referred to the web version of this article.)

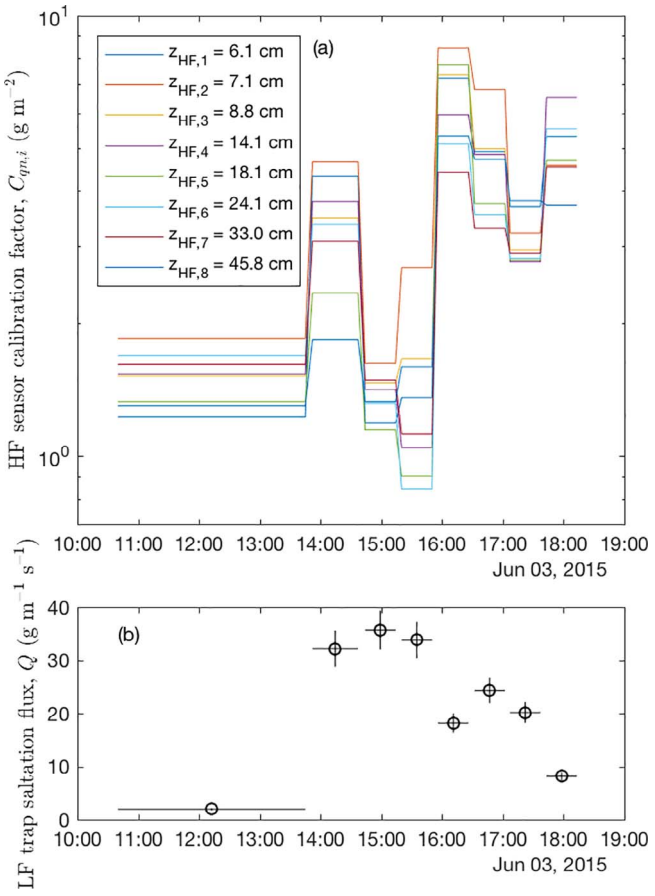

Fig. 6. (a) Example of variation through time in calibration factors $C_{qn,i}$ for HF sensors i at heights $z_{HF,i}$ above the bed surface, calculated for 3 October 2017 at the Oceano field site. Values of $C_{qn,i}$ adjust over discrete time intervals associated with LF trap saltation measurements. (b) Variation through time in the total saltation flux Q for LF saltation trap profiles. Horizontal bars indicate LF trap measurement time intervals. Q values for each of these intervals are calculated through application of the fitting method (described in Section 4.4.1 below) to vertical profiles of LF trap height-specific fluxes $q_{LF,i}$; vertical bars indicate uncertainties in Q values for these intervals.

measurement time interval to predict height-specific saltation fluxes $q_{pred,HF,i}$ for each HF sensor i at height $z_{HF,i}$ over this same time interval (Fig. 5a). Second, we determine time-averaged count rates $n_{cal,HF,i}$ for each HF sensor over these calibration time intervals (Fig. 5b). Third, we compute the ratio of $q_{pred,HF,i}$ and $n_{cal,HF,i}$ to obtain calibration factors $C_{qn,i}$ (Fig. 5c).

We first obtain the expected height-specific horizontal saltation flux $q_{pred,HF,i}$ at sensor height $z_{HF,i}$ based on the LF exponential profile fit parameters $q_{0,LF}$ and $z_{q,LF}$ for that time interval. This method, which is illustrated in Fig. 5a, assumes that the exponential flux profile, established for the LF traps mostly higher above the bed surface, can be extrapolated downward to the HF sensors closer to the surface, where height-specific saltation flux may in fact diverge from the exponential expectation (e.g., Bauer and Davidson-Arnott, 2014):

$$q_{pred,HF,i} = q_{0,LF}\exp\left(-\frac{z_{HF,i}}{z_{q,LF}}\right). \quad (4)$$

$q_{pred,HF,i}$ thus represent expectations for long-term saltation fluxes at HF sensor heights derived from LF trap measurements. We consider the validity of such expectations in Section 5.1.2. In Supporting Information Section S1.7, we describe methods for computing the HF sensor heights $z_{HF,i}$, which depend on bed elevation measurements from laser distance sensors mounted with HF sensors, and we provide details for computing the associated uncertainty in expected saltation fluxes $\sigma_{q_{pred,HF,i}}$ in Supporting Information Section S1.8. Then, in Supporting Information Section S1.9, we describe specific calculations to address the wide spanwise separation among LF traps at Oceano, where we obtain $q_{0,LF}$ and $z_{q,LF}$ as a combination of two sets of profile fit parameters.

After obtaining $q_{pred,HF,i}$, we next determine the particle count rate $n_{cal,HF,i}$ for each HF sensor i over the corresponding LF trap measurement interval of duration T_{LF} (Fig. 5b):

$$n_{cal,HF,i} = N_{cal,HF,i}/T_{LF}, \quad (5)$$

where $N_{cal,HF,i}$ is the total number of particles counted by HF sensor i during T_{LF}. We note here that the extended duration of T_{LF} (typically 30 min), assumes a steady saltation profile shape during each calibration interval. This assumption is supported by observations that the time-averaged saltation layer height does not vary with wind strength (Martin and Kok, 2017a); however, as we consider in Section 5.1.2, variations in saltation profile shape over times less than T_{LF} could affect our calibration process (e.g., Bauer and Davidson-Arnott, 2014).

Finally, based on the expected height-specific horizontal saltation flux $q_{pred,HF,i}$ and number count rate $n_{cal,HF,i}$ for each HF sensor i, we estimate the calibration factor for each HF sensor as:

$$C_{qn,i} = \frac{q_{pred,HF,i}}{n_{cal,HF,i}}. \quad (6)$$

Methods for estimating the associated calibration factor uncertainty $\sigma_{C_{qn,i}}$ are described in Supporting Information Section S1.10.

4.2.3. Evaluation of flux calibration factors

We note that HF sensor calibration factors varied substantially through time, due to a variety of possible factors. These include variation in ambient light and the buildup of scratches, dust, and condensation on sensor lenses. Subtle changes in wind direction, which affected the alignment of fixed HF sensors with respect to rotating LF traps, may have also contributed to variations in calibration factors. Though we lack specific measurements from our optical sensors, such as time series of signal intensity, which could help to isolate the individual factors contributing to variation in calibration factors, we believe that our calibration method is able to reasonably account for all factors contributing to variation in sensor performance and alignment.

To further evaluate our calibration method, we perform a qualitative examination of variation in calibration factors through time. We consider measurements from a single day (3 June 2015) at a single site (Oceano) for which we have a large number of LF trap profiles (8), a wide range of saltation conditions, and a long continuous record of HF sensor measurements (> 7 h). For these sample measurements, Fig. 6 shows that there is substantial variation in calibration factors across sensors and time intervals throughout the day. Much of the variation in $C_{qn,i}$ appears to be correlated among all sensors, but such synchronous variations appear unrelated to variations in saltation flux measured by the LF traps. It is possible that, by neglecting high-frequency variations in the bed elevation, we are failing to account for systematic variations in the HF sensor heights, which could drive synchronous variations in $C_{qn,i}$ for all sensors.

Another factor that could have contributed to variation in calibration factors was the mounting of LF traps in a freely rotating orientation versus HF sensors in a fixed orientation. Such mounting differences could have caused significant variation in the ratio of saltation fluxes measured by wind-aligned LF traps and partially wind-oblique HF sensors. To assess this, we examine how observed calibration factors vary with both the mean and the standard deviation of wind direction during individual calibration intervals (Supporting Information Fig. S6). At Rancho Guadalupe, $C_{qn,i}$ shows no variation with wind direction, but $C_{qn,i}$ does decline significantly with the mean (Fig. S6a) and standard deviation (Fig. S6b) of wind direction at Jericoacoara and Oceano. In these cases, wind direction variability does appear to contribute some additional uncertainty to the HF sensor calibration. However, the

observed decline in $C_{qn,i}$ with increasing wind angle suggests increasing sensitivity of HF sensors to the passage of saltating particles, which contrasts with an expected decrease in HF sensor sensitivity due to the increasingly oblique wind direction with respect to the sensors. Therefore, other difficult-to-quantify factors related to wind direction may be driving calibration factor variability.

Additional, but less substantial, variation in $C_{qn,i}$ appears related to variation among individual sensor heights. We expect that some of the variation in $C_{qn,i}$ could be explained by variation of airborne particle sizes, because pulse counts from coarser particles represent a greater saltation mass flux than those from finer particles. In particular, assuming spherical particles, we expect that the calibration factor $C_{qn,pred,i}$ for trap i will be:

$$C_{qn,pred,i} = \frac{\frac{\pi}{6}\rho_s \overline{d}^3}{A_{HF}} \tag{7}$$

where ρ_s is particle density, assumed as 2650 kg/m^3 for natural sand, $\overline{d}$ is the volume-weighted mean diameter of particles passing through the HF sensor, and $A_{HF} = 18$ mm^2 is the area of the sensor opening, approximated for the Wenglor as the product of the sensor's 30 mm path length and 0.6 mm laser beam diameter. In general, we observe a subtle increase in $\overline{d}$ with height above the bed surface; thus, we also expect $C_{qn,pred,i}$ to increase with height.

Both the observed ($C_{qn,i}$; Fig. 7a) and predicted ($C_{qn,pred,i}$; Fig. 7b) calibration factors show a weak increase with height, lending support to the grain-size dependence of the calibration factors, similar to that discussed by Barchyn et al. (2014a). Furthermore, when directly comparing observed and predicted calibration factors (Fig. 7c), we find a general similarity in values. However, we also find substantial differences in observed and predicted calibration factors, suggesting the presence of other factors contributing to calibration factor variability. As discussed above, systematic variation in HF sensor heights and variation in wind direction could both play a role in this. Other possible factors affecting calibration variability include: intensity of the emitted laser beam, variation in ambient sunlight, clarity of the lenses, shape and orientation of particles passing through the beam, and optical properties of particles (Barchyn et al., 2014a). In general, though, the adoption of our calibration technique avoids the need to ascribe specific explanations to variations in HF sensor sensitivities through time.

We also evaluated the possibility that HF sensor saturation (i.e., reaching a maximum count rate), could affect the calibration factors. To do so, we examined all calibration factors $C_{qn,i}$ versus the number counts $n_{cal,HF,i}$ for all HF sensors i for all calibration intervals (Supporting Information Fig. S7). Were saturation to occur, we would expect an increase in $C_{qn,i}$ for large $n_{cal,HF,i}$, corresponding to undercounting of particles. We do indeed note a slight but significant increase in $C_{qn,i}$ with $n_{cal,HF,i}$ at Jericoacoara and Oceano, but this increase only accounts for a small fraction of the variability in $C_{qn,i}$. In fact, for large $n_{cal,HF,i}$ (>100 s^{-1}), there appear to be a few cases of unusually small $C_{qn,i}$, indicating either an overcounting of particles or an underprediction of the saltation flux during the calibration interval. Notably, these cases are all associated with small values of $z_{HF,i}$, suggesting the possibility that these HF sensors are embedded in a near-surface region in which saltation flux is enhanced beyond the exponential expectation (Namikas, 2003; Bauer and Davidson-Arnott, 2014). Thus, while there may be some bias in calibration factors related to variation in the saltation flux, such bias is unlikely related to sensor saturation.

4.3. Subsampling high-frequency (HF) saltation flux profiles

In this subsection, we describe methods for calibrating and combining saltation number counts from HF sensors to obtain height-specific horizontal saltation flux profiles $q_i(z_i)$ over arbitrary subsampling time intervals Δt, and we address the occurrence and treatment of zero flux values in these profiles. By obtaining these saltation profiles, we can estimate total saltation fluxes Q, saltation layer heights z_q, and other profile parameters, as we will describe later in Section 4.4.

4.3.1. Calculation of height-specific saltation fluxes for HF sensors

Given a subsampling time interval Δt, we compute count rates n_i for each HF sensor i as the total measured particle counts divided by Δt. We then apply Eq. (3) to convert each n_i into a calibrated height-specific horizontal saltation flux q_i, using the calibration factor $C_{qn,i}$ obtained for the concurrent LF time interval, as illustrated in Fig. 8. Methods for estimating the associated calibrated height-specific horizontal saltation flux uncertainty σ_{q_i} are described in Supporting Information Section S1.11.

4.3.2. Occurrence and treatment of zero values in vertical flux profiles

In certain instances, some, but not all, of the HF sensors registered zero particle counts (i.e., $n_i = 0$) and thus zero calibrated flux ($q_i = 0$). However, performing exponential fits to $q_i(z_i)$ (see Section 4.4 below) requires first calculating $\log(q_i)$, which is not possible for $q_i = 0$. This is generally a minor issue over long averaging time intervals Δt, for which

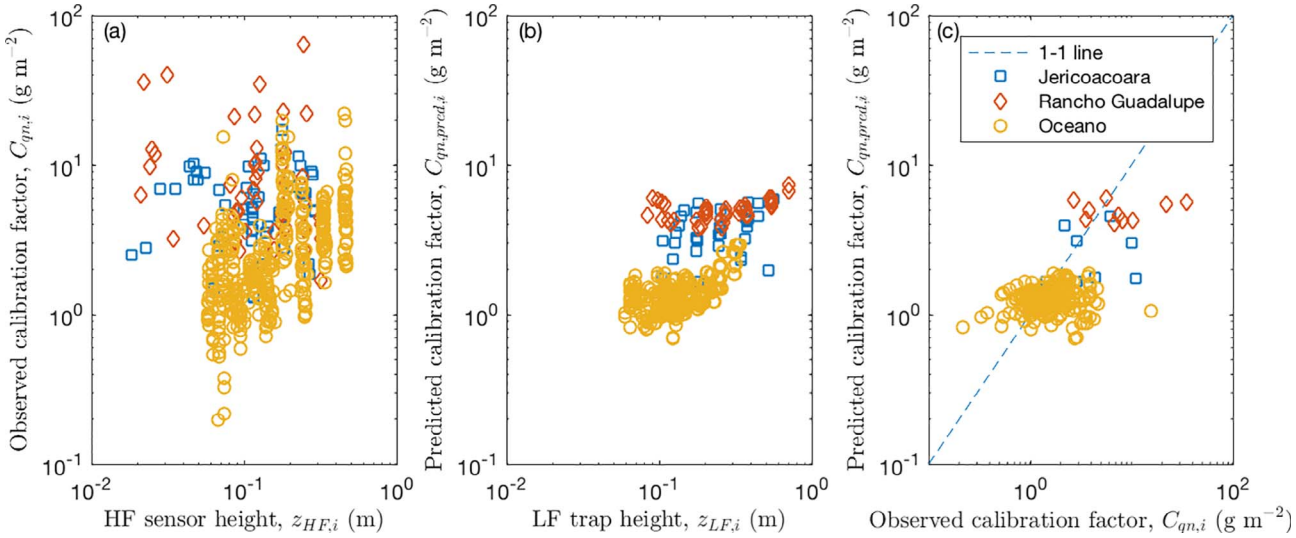

Fig. 7. (a) Observed calibration factor $C_{qn,i}$ versus HF sensor height $z_{HF,i}$ (Eq. (6)). (b) Variation in expected calibration factor $C_{qn,pred,i}$ (Eq. (7)) versus LF trap height $z_{LF,i}$. (c) Direct comparison of observed and predicted calibration factors. Due to differences in trap heights versus sensor heights, only a limited number of data points (with similar heights) are included in this plot.

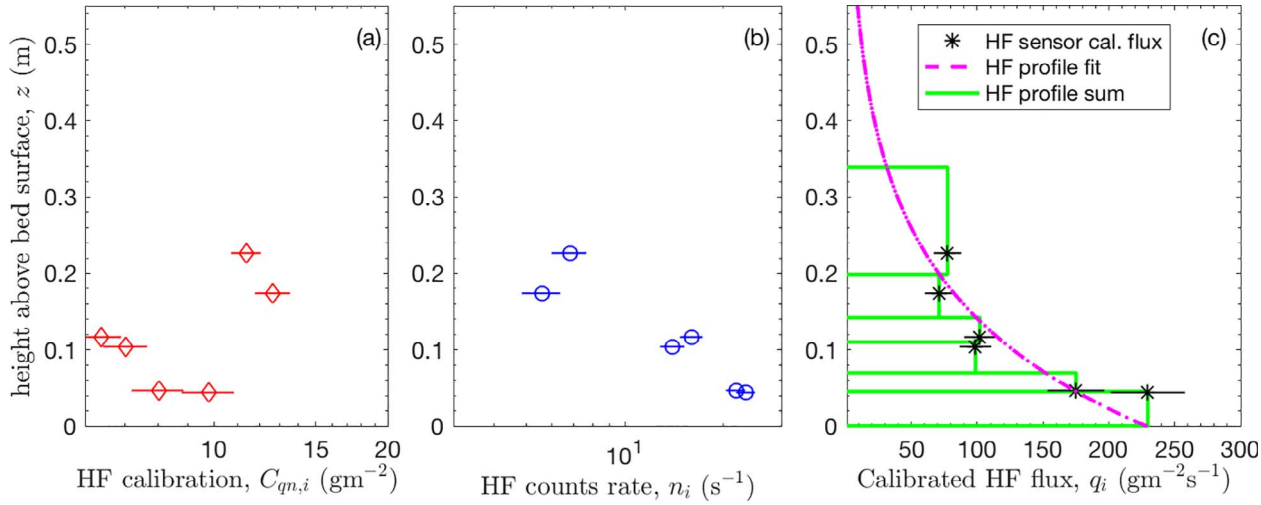

Fig. 8. Demonstration of the three primary steps in the method for computing and fitting saltation flux for a profile of HF sensors for a $\Delta t = 10$ s subsampling interval, as detailed in Sections 4.3 and 4.4. The data are from Jericoacoara on 14 November 2014, from 15:26:00 to 15:26:10 local time. (a) First, we obtain the calibration factors $C_{qn,i}$ from the corresponding LF trap time interval (i.e., Fig. 5c). (b) Second, we compute the HF sensor count rates n_i for the $\Delta t = 10$ s subsampling interval (blue circles). (c) Third, we compute calibrated saltation fluxes q_i over Δt as the product of $C_{qn,i}$ and n_i by Eq. (3) (black asterisks). To estimate the total saltation flux Q, we can either apply the profile fitting method (dashed magenta line – Section 4.4.1) or the summation method (green bars – Section 4.4.2) for the profile of q_i. (For interpretation of the references to colour in this figure legend, the reader is referred to the web version of this article.)

all sensors register particle counts. However, for small Δt, weak saltation, or sensors far above the surface, instances of $q_i = 0$ are common.

In Fig. 9, we examine the occurrence of zero values in saltation flux profiles. Fig. 9a shows how, at our Oceano field site, the incidence of $q_i = 0$ increases with decreasing sampling time scale Δt. Zero values are less of an issue at Jericoacoara and Rancho Guadalupe, where saltation tended to be stronger and HF sensors were closer to the surface. To control for these effects, we consider in Fig. 9b the occurrence of $q_i = 0$ for a fixed height z_i and fixed sampling time scale Δt as a function of wind speed, u. When controlling for these factors, HF sensors at all sites have a comparable rate of incidence of zero flux values.

Flux profiles with zeros are problematic for profile fitting. The simplest approach would be to simply exclude from analysis those time intervals for which at least one $q_i = 0$. However, doing so could preferentially exclude time intervals of weak saltation, thus reducing the data available for analysis and biasing the results from these analyses. An alternative approach is to exclude from analysis only those individual sensors with $q_i = 0$, but to continue with profile fitting to the remaining sensor heights with $q_i > 0$. Such selective inclusion of sensors is possible if there are at least three measurements available to perform exponential fits and compute uncertainties. However, such selective inclusion of certain sensor heights may bias vertical profile fits.

Fig. 10 considers these two approaches to the treatment of zero values in exponential profile fits at a variety of sampling time scales Δt. For each time interval with at least three HF heights for which $q_i > 0$, we perform an exponential profile fit to obtain a value for the saltation layer height z_q. Then, we follow two approaches to compute the average and uncertainty of z_q values for a single site and Δt: first, we include only "full" profiles in this averaging (i.e., profiles for which all $q_i > 0$), and second, we include all profiles in this averaging (except for profiles with fewer than three $q_i > 0$, the minimum required for fitting). For the most part, there is no difference in these two methods for treating zero values, which occur very infrequently at Jericoacoara and Rancho Guadalupe and for large Δt at Oceano. However, for small Δt at Oceano, z_q values from only full profile are larger than values from all profiles and diverge from values computed at longer time scales. This

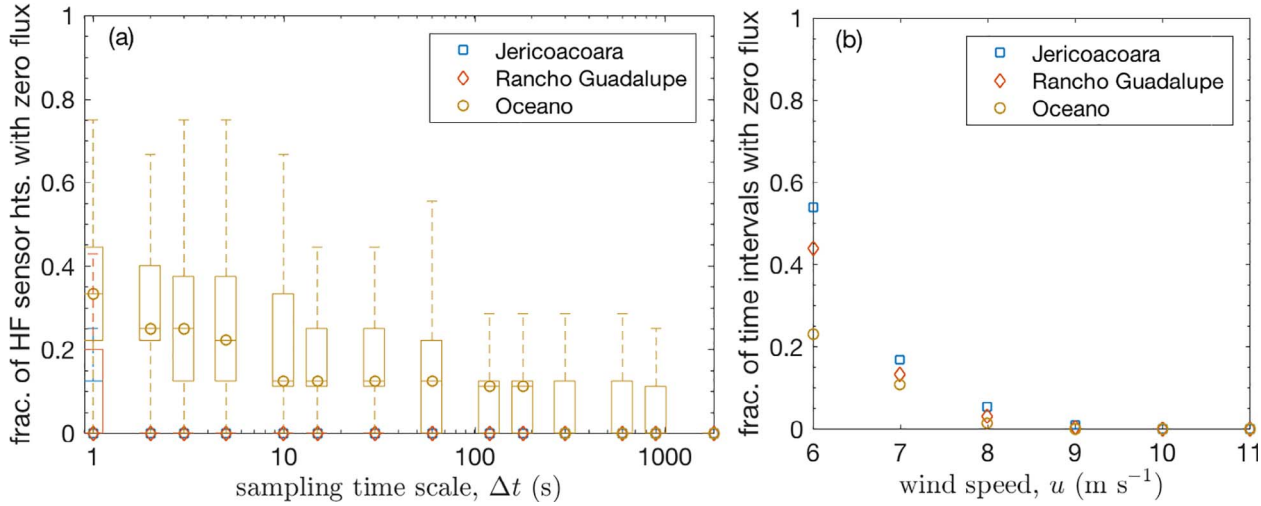

Fig. 9. (a) Box plot describing the number of heights within the HF sensor profile for which height-specific saltation flux q_i equals zero, as a function of time scale at each field site. Boxes indicate the range from 25th to 75th percentile values, and bars indicate the full range. For Jericoacoara and Rancho Guadalupe, most of the values are 0. (b) For a specific sensor height, $z_{HF,i}/z_q \approx 2$, and specific sampling interval $\Delta t = 5$ s, the fraction of time intervals for which q_i equals zero, as a function of wind speed u.

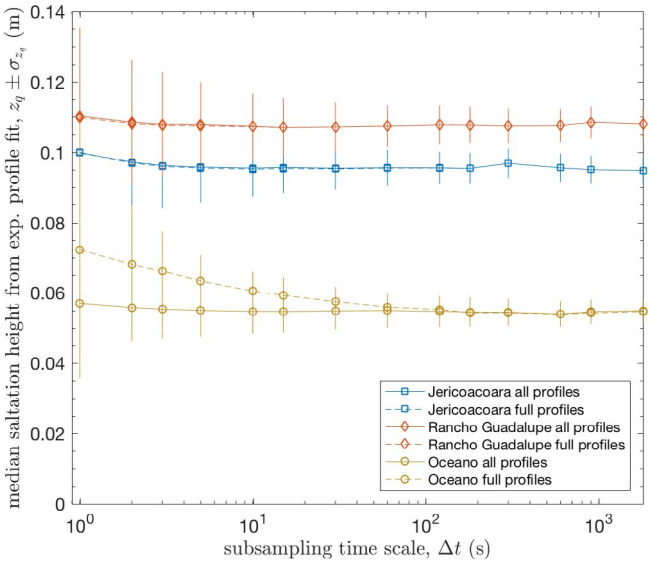

Fig. 10. Median values of saltation layer height z_q (symbols) and fitting uncertainty σ_{z_q} (bars) for exponential fits to profiles of height-specific saltation flux q_i from HF sensors, versus subsampling time scale Δt. Solid lines denote median z_q computed from all flux profiles; dashed lines denote median z_q computed only from "full" flux profiles for which $q_i > 0$ at all sensor heights.

may occur because full profiles are biased toward instances where the height-specific saltation flux near the top of the saltation profile is larger than would normally be expected. In particular, for a small Δt, there is a minimum detectable nonzero q_i that may exceed the actual height-specific saltation flux at HF sensor heights near the top of the profile, which skews the z_q of these full profile fits toward larger values. As Δt then increases, the minimum detectable nonzero q_i decreases until such biasing is no longer an issue. Given this biasing effect, we choose instead to follow the approach of fitting to all possible vertical profiles of saltation flux, and to simply exclude single $q_i = 0$ values from these profile fits when necessary.

4.4. Estimation of total (vertically-integrated) saltation flux

In this subsection, we describe methods for estimating the total saltation flux Q by integrating over the vertical profiles of height-specific saltation flux $q_i(z_i)$ at arbitrary Δt. For these analyses, we follow the steps described in Section 4.3 above to obtain the $q_i(z_i)$ profiles. This includes using all flux profiles regardless of the existence of $q_i = 0$ within the profile, so long as there are at least 3 nonzero flux values for fitting the profile. Based on these profiles, we estimate the total flux as follows:

$$Q = \int_{z=0}^{z=\infty} q(z)\, dz. \tag{8}$$

Because we have only a limited number of $q_i(z_i)$ data points, calculation of Q requires some approximations. In particular, we here assume an exponential profile for $q(z)$ (see Supporting Information Section S1.6), thus:

$$Q = \int_{z=0}^{z=\infty} q_0 \exp(z/z_q)\, dz \tag{9}$$

We consider two different methods for computing Q, as we describe below. In the first method, described in Section 4.4.1, we perform exponential profile fits to each $q_i(z_i)$ profile, then we use the resulting profile fit parameters q_0 and z_q to estimate the total flux Q. In the second method, described in Section 4.4.2, we obtain the total flux Q by computing a sum of all of the q_i, weighted according to their expected contributions to the exponential profile. Though requiring a greater number of assumptions to compute, the summation method allows Q to be estimated at all time steps and all time scales Δt, regardless of the occurrence of $q_i = 0$ or other issues limiting an exponential profile fit.

4.4.1. Total flux estimation by exponential profile fit method

Given nonzero height-specific saltation fluxes q_i at heights z_i, we perform exponential profile fits to obtain profile fit parameters q_0 and z_q. Calculating the integral in Eq. (9), we then obtain the total flux as:

$$Q_{fit} = q_0 z_q. \tag{10}$$

We calculate the associated uncertainty in Q_{fit} through error propagation (see Supporting Information Section S1.12).

This method for obtaining Q_{fit} assumes the ability to fit an exponential profile to the respective calibrated values of q_i and z_i. When all of the q_i equal 0, we assume that $Q_{fit} = 0$. Otherwise, for time increments with some nonzero $q_i > 0$, but with an insufficient number of these nonzero q_i to perform an exponential fit (i.e., fewer than 3), the value for Q_{fit} remains undefined. In cases of small Δt or weak saltation, such undefined Q_{fit} often constitute a substantial fraction of the time increments, hindering time series analyses for $Q_{fit}(t)$. To avoid this problem, the next section presents an alternative "weighted sum" approach to estimating the total, vertically-integrated, saltation flux.

4.4.2. Total flux estimation by weighted sum method

Over very short time increments Δt, performing the fit to obtain q_0 and z_q for the site may be difficult if a large number of q_i in the profile equal 0, or if the profile has not yet converged to its exponential form. In these cases, based on our observation that z_q remains roughly invariant at each site, we can instead compute Q as a weighted sum:

$$Q_{sum} = \sum_i \Delta Q_i, \tag{11}$$

where ΔQ_i is an incremental contribution to the total flux from q_i, weighted by the relative vertical coverage of q_i in the profile. We compute ΔQ_i as:

$$\Delta Q_i = \int_{z_{i,bot}}^{z_{i,top}} q_{0,i} \exp\left(-\frac{z}{z_{q,LF}}\right) dz = q_{0,i} z_{q,LF} \left[\exp\left(-\frac{z_{i,bot}}{z_{q,LF}}\right) - \exp\left(-\frac{z_{i,top}}{z_{q,LF}}\right)\right], \tag{12}$$

where $z_{i,bot} = \sqrt{z_i z_{i-1}}$, and z_{i-1} is the height of the HF sensor below z_i; if z_i is the lowest, then $z_{i,bot} = 0$. $z_{i,top} = \sqrt{z_i z_{i+1}}$, and z_{i+1} is the height of HF sensor above z_i; if z_i is the highest, then $z_{i,top} = \infty$. $q_{0,i}$ is an equivalent value for q_0 determined based on q_i, as:

$$q_i = q_{0,i} \exp\left(-\frac{z_i}{z_{q,LF}}\right); \tag{13}$$

i.e., $q_{0,i}$ is the expected value of q_0 given an exponential profile with $q_i(z_i)$ and $z_{q,LF}$. In Eqs. (12) and (13), we use a saltation layer height equal to $z_{q,LF}$, i.e., the value obtained from the LF trap measurements prior to the calibration of the HF sensors. We calculate the uncertainty in Q for the summation method through error propagation (see Supporting Information Section S1.13).

This summation method for obtaining Q has the distinct advantage that it does not require convergence of the $q_i(z_i)$ profile to an exponential form, which can be an issue for fits applied to $q_i(z_i)$ at very small sampling time scales Δt. However, calculation of Q by the summation method must assume a constant saltation layer height $z_{q,LF}$, whereas calculation of Q by the exponential fitting method accounts for changes in z_q over time. This limitation of the summation method is acceptable because z_q appears to remain approximately constant regardless of wind conditions and calculation time scale (Fig. 10 and Martin and Kok, 2017a).

4.4.3. Comparison of fitting and summation methods for estimating total saltation flux

In Fig. 11a we compare total saltation fluxes computed by the two

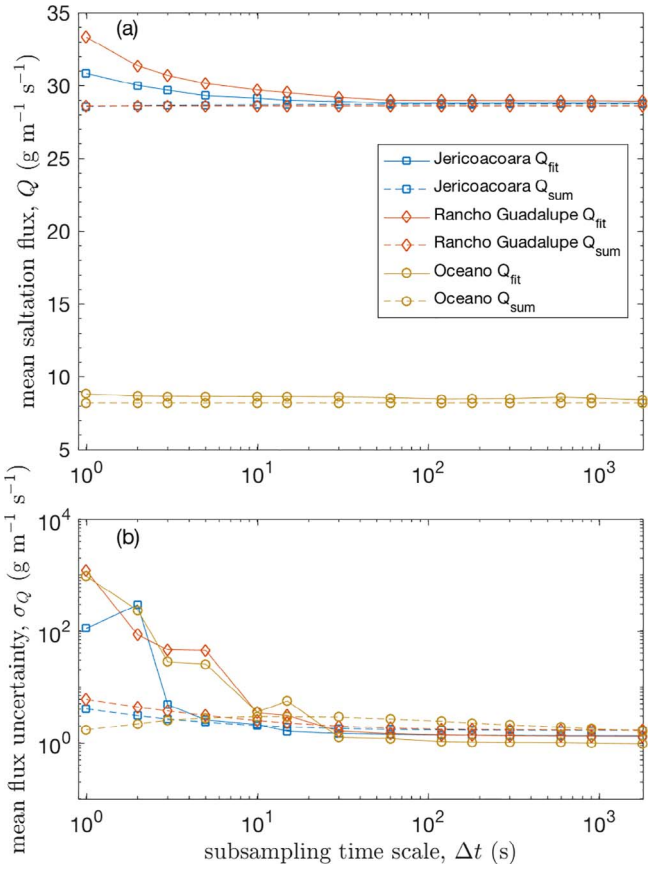

Fig. 11. (a) Mean values for total saltation flux estimated by exponential profile fitting method Q_{fit} (Eq. (10)) versus summation method Q_{sum} (Eq. (11)). (b) Mean of uncertainty in exponential fit flux $\sigma_{Q_{fit}}$ (Supporting Information Eq. (S39)) and summation flux $\sigma_{Q_{sum}}$ (Supporting Information Eq. (S42)).

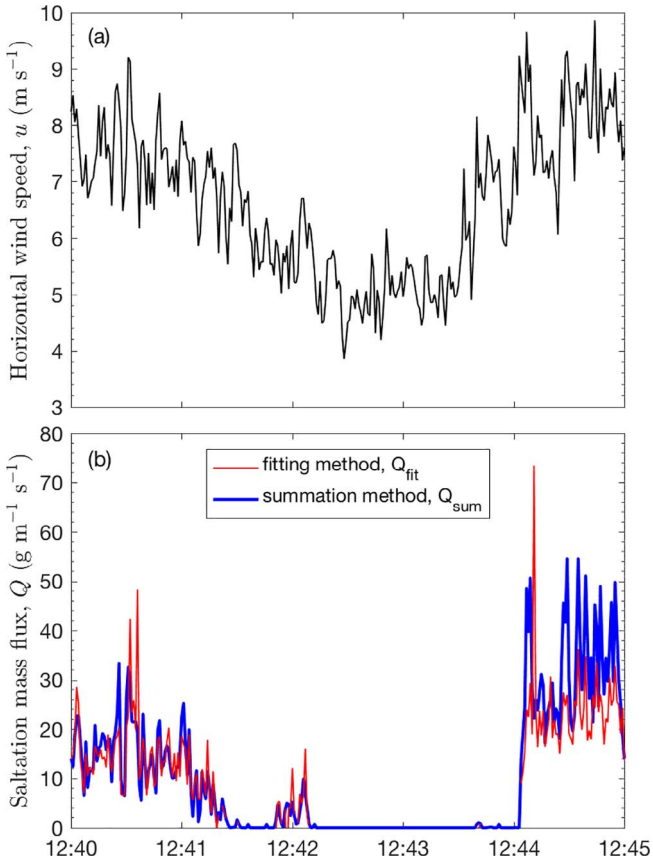

Fig. 12. Sample time series of (a) streamwise wind speed u, and (b) total saltation mass flux Q by fitting (Eq. (10)) and summation (Eq. (11)) methods calculated over $\Delta t = 1$ s increments. The data are from Oceano on 16 May 2015, from 12:40 to 12:45 local time. Time increments with missing red curve indicate undefined values for Q by the fitting method. (For interpretation of the references to colour in this figure legend, the reader is referred to the web version of this article.)

methods, Q_{fit} and Q_{sum}, as a function of sampling time scale Δt. We find that Q_{sum} remains constant with Δt, indicating that summation is a reliable way to estimate the total saltation flux regardless of time scale. In contrast, Q_{fit} increases with decreasing Δt for $\Delta t \lesssim 30$ s, indicating the unreliability of such exponential fits at short times scales. This breakdown in exponential fits for small Δt is likely related to a breakdown – either in actuality or due to the increase in statistical noise at small time scales – in exponential flux profile fitting at short time scales. Actual breakdown of the exponential flux profile may occur at short time scales due to the presence of turbulence structures causing short-term variations in profile shape. Though such profile variations are indeed likely, the fact that mean Q_{sum} remains constant regardless of Δt indicates that there are no systematic changes in profile shape at short time scales. Instead, it is most likely that measurement effects – i.e. counting uncertainty and the presence of zero values in sensor number counts at short time scales – causes the breakdown in estimates of Q_{fit}. Notably, uncertainties in Q_{fit} and Q_{sum} display trends similar to the flux values themselves (Fig. 11b). The divergence of Q_{fit} from Q_{sum} (and the associated uncertainties for these values) as Δt becomes small suggests increasing error due to the breakdown of exponential fitting for measurements obtained at short time scales of less than 30 s.

4.4.4. Illustration of calibrated high-frequency saltation flux time series

Though this paper is mostly focused on the methodology for characterizing high-frequency saltation flux, it is illustrative to examine how measured variations of saltation flux are related to measured variations of wind speed. As a basis for making the comparison between saltation and wind, we briefly describe here our methods for measuring wind speed properties, and we refer interested readers to examine these details further in Martin and Kok (2017a). For all wind calculations, we first subdivided raw wind data into 30-min time intervals. For each of these 30-min intervals, we then performed a streamline correction to align the measured wind values with the mean streamwise wind $\overline{u}$, such that mean transverse $\overline{v}$ and vertical $\overline{w}$ winds equaled zero over each interval. Here, we consider only the streamline-corrected streamwise wind speed u.

A sample time series illustrating fluctuations in measured wind speed and saltation flux is shown in Fig. 12. This time series demonstrates the typical variability of streamwise winds u, which give rise to variations of total saltation flux Q. To first order, both the fitting and summation methods produce similar time series of Q. However, the fluctuations of Q_{sum}, which are not subject to noisy variations in the profile fitting process, tend to display smaller fluctuations than the values of Q_{fit}. Fig. 12 also shows that a small number of time increments only produce a value for Q_{sum} but not for Q_{fit}. These gaps in Q_{fit} occur when the exponential fitting fails, either due to a large number of zero q_i values in the profile or a fitting to the remaining nonzero q_i that fail to produce a real number for Q.

5. Discussion

We have presented a new methodology for determining the high-frequency variability of saltation flux under natural field conditions. We have shown that calibrated, height-specific saltation fluxes can be obtained at arbitrary time scales through the deployment of low-frequency (LF) saltation traps and high-frequency (HF) saltation sensors. We have further addressed high-frequency profile fitting issues by

offering a summation method for the total saltation flux that is unaffected by the occurrence of poor profile fits at short time scales. This methodology, therefore, offers a novel way to directly compare high-frequency variations of wind speed and the total saltation flux, which can inform advances in understanding the two-way interactions between saltation transport and driving turbulent winds.

In this Discussion, we compare our work with past attempts to characterize high-frequency variability of saltation flux, examining in particular how the new methodology addresses some, but not all, of the limitations of past work. Based on these considerations, we offer recommendations for future work to measure high-frequency variability of total saltation flux. We also explore some opportunities for addressing outstanding problems in aeolian research offered by our new methodology.

5.1. Comparison to previous high-frequency (HF) saltation characterization

The instruments used in our field deployments are not new to the study of aeolian saltation. The innovation of our work lies in the way we have combined these instruments, as the coupled use of LF traps and HF sensors in studies of aeolian saltation is rare (Martin et al., 2013). Past field-based studies examining high-frequency variability of aeolian saltation flux have typically only considered relative, and not absolute, variations of flux. When attempts have been made to convert HF number counts to absolute saltation fluxes, these studies have typically relied on extensive grain size measurements (Barchyn et al., 2014a), required theoretical conversion factors (Bauer and Davidson-Arnott, 2014) or used pre-determined empirical calibration factors (Nield et al., 2017). In contrast, our methodology employs a field-based calibration of HF sensor counts, which is directly tied to the specific conditions of the instruments and the field site. In the following subsections, we further consider the advancements of our methodology over past work, after which we describe some remaining limitations.

5.1.1. Advances over past work

One important element of our field-based empirical calibration procedure is that it allows for changes in the calibration factor through time, thus accommodating the issue of HF sensor drift observed in this and past studies (e.g., Bauer et al., 2012). These sensor drift issues appear to be most pronounced for optical sensors, such as the Wenglors used here (Hugenholtz and Barchyn, 2011), and for acoustic sensors like the Miniphone (Ellis et al., 2009b). For extended field deployments such as ours, application of our calibration methodology avoids the need to replace HF saltation sensors each time there is a slight degradation in sensor consistency. Our calibration methodology therefore provides a practical way to construct reliable HF saltation time series with imperfect optical sensors, despite their limitations (see Section 5.1.2. below). Alternatively, piezoelectric impact sensors could be used to avoid calibration drift issues; however, strong momentum/sampling area dependencies of these sensors present additional issues for HF saltation flux characterization (Hugenholtz and Barchyn, 2011).

In addition to advancing methods for calculating HF height-specific saltation fluxes, we have also provided here new methods for obtaining HF time series of the total (vertically-integrated) saltation flux through a summation method that is unaffected by profile fit issues that arise at short time scales. In contrast, previous HF time series of total saltation flux typically depended only on saltation measured at a single height (e.g., Baas and Sherman, 2005). Based on the assumption, supported by observations, that the saltation layer is insensitive to changes in observational time scale (Fig. 10) or changes in wind conditions (Martin and Kok, 2017a), our summation method provides continuous time series of total saltation flux regardless of the intensity of saltation or the time scale of HF time series interval averaging.

5.1.2. Remaining limitations

Though useful for exploring many aspects of saltation mechanics, our methodology for characterizing high-frequency saltation flux depends on several assumptions, which limit its applicability in certain cases. These assumptions include the accuracy of LF trap measurements, negligible HF sensor drift within calibration intervals, spatial homogeneity within the deployment domain, and constant flux profile shapes during averaging intervals.

We assume that LF saltation traps provide accurate and consistent measurements of saltation flux through time; however, studies have indicated the possibility that saltation trap efficiency may vary with airflow conditions and saltation intensities (Goossens et al., 2000; Sherman et al., 1998). Such biases could produce height-dependent relative errors in the LF profiles for $q(z)$, and thus systematic errors in the calibration factors used to obtain HF fluxes. Such problems are not unique to the calibration of HF measurements, and they will affect all saltation studies using LF traps.

Our calibration methodology further assumes negligible HF sensor drift during individual calibration intervals. It thus requires vigilant data quality control checks to ensure that excessively drifting HF sensor outputs, i.e., those showing anomalous changes in particle count rates compared to other sensors, are not included in saltation flux calculations. However, detecting and eliminating all such malfunctioning HF sensors is difficult. Sensor drift detection also depends on assuming a linear relationship between measured particle counts and the actual saltation flux. Though such linearity is supported for Wenglors by the experiments of Barchyn et al. (2014a), it must be tested before using other HF sensors for calibration (see Section 5.2.2 below). In the future, increasing the number of HF sensors in a deployment may help to better identify anomalous sensor drift.

In performing our calibration, we also assume spatial homogeneity within the footprint of HF and LF flux measurements. By making this assumption, we are able to relate time-averaged LF trap vertical profiles of saltation flux to HF sensor vertical profiles of particle counts. However, it is possible that, for spatially-separated LF and HF measurements, these profiles are not in fact measuring the same saltation flux. Indeed, at Oceano, where LF vertical profiles were separated in the spanwise direction by ~ 9 m, we did observe significant profile differences (Supporting Information Fig. S3), possibly reflecting the presence of different surface or wind conditions. Because our HF measurements were situated at the halfway point between these two LF profiles, we use the average of the two LF profiles for calibration of the HF particle counts (Supporting Information Section S1.9 and Fig. S3). This spanwise separation of LF profiles is likely reflected in the larger uncertainty of HF calibration factors at the Oceano site. Furthermore, our estimation of vertically-integrated saltation flux over very short (i.e., $T \leqslant 1$ s) intervals may be disrupted by turbulence-driven variations in the flux arising from the small but significant separation between HF sensors. Due to these potential issues of spatial heterogeneity, our saltation calibration methods are unable to resolve spatial variability of saltation flux at length scales shorter than the spatial extent of combined LF and HF instrument setups.

Finally, we assume that vertical profiles of saltation flux follow an exponential form, with approximately constant saltation layer heights. We invoke the exponential profile at three points in our analysis: first, to fit the LF saltation flux profile; second, to predict time-integrated saltation fluxes at the heights of the Wenglors; and third, to fit the subsampled vertical profiles of HF saltation flux. For these exponential profiles, we assume constant saltation layer heights when computing uncertainty in profile fits and when weighting the relative contributions of individual HF sensors to the total saltation flux by the summation method. Our direct observation of exponential flux profiles (see Supporting Information Section S1.6) and past work indicating constant saltation heights that do not vary with wind strength (Martin and Kok, 2017a) support our application of constant-shape exponential profiles; however, other observations indicate variations of saltation profile shape through time (Bauer and Davidson-Arnott, 2014). Profile shape variation seems to occur at time intervals somewhat shorter than our LF

trap collection times (i.e., $T \approx 15$ min), and shape variation seems to be most pronounced near the surface (i.e., $z < 2$ cm), where reptation and creep contribute significantly to the total sand flux (e.g., Namikas, 2003; Bauer and Davidson-Arnott, 2014). Due to the bulkiness of our LF traps and the operational failure of our HF sensors close to the surface, we were unable to obtain reliable saltation measurements in this near-surface zone, within which past measurements suggest that height-specific fluxes are larger than expected from the exponential profile (Namikas, 2003; Bauer and Davidson-Arnott, 2014). By excluding near-surface sensors, it is therefore possible that our estimates of total saltation flux Q, both by the fitting and summation methods, may be less than the actual total sand flux (including saltation, reptation, and creep). Further work is needed to develop robust HF saltation flux sensing methods close to the bed surface and to verify the quality of near-surface LF trap measurements for calibration of HF fluxes.

5.2. Recommendations for field work to characterize high-frequency (HF) saltation variability

Based on the innovations and limitations of our methodology for characterizing HF saltation flux variability, we now present recommendations for future field deployments to obtain quality HF saltation flux measurements. These recommendations include selection of instruments, strategies for deploying these instruments, and methods for processing LF and HF saltation data. Our recommendations are not meant to provide an authoritative endorsement of specific saltation traps and sensors. Rather, we hope to convey the main criteria for selecting, arranging, and utilizing saltation sensors for future field deployments. An overview of our instrumentation recommendations is provided in Table 2. We refer readers to Zobeck et al. (2003) for broader considerations regarding the siting and design for field studies of active aeolian saltation and wind erosion.

5.2.1. Low-frequency (LF) instrument selection

In our methodology for characterizing high-frequency (HF) saltation fluctuations, the role of the LF saltation traps is to provide vertical profiles of saltation flux in absolute mass flux units. Therefore, a key concern is that the LF traps provide reliable mass fluxes over the sampling intervals of interest. The reliability of some LF traps was evaluated by Goossens et al. (2000). They found that, among the four most commonly used saltation traps at that time, Modified Wilson and Cook (MWAC) traps provide the most consistent absolute measurements of saltation flux across a range of grain sizes and wind speeds, and that Big Springs Number Eight (BSNE) traps also provide reasonably consistent saltation fluxes, with high collection efficiency for all but the smallest (~132 um) particle size classes. Thus, we believe that the LF traps deployed in our study provided reliable flux profiles for medium and coarse particles, but less reliable measurements for saltation of the finest particles. Aside from the saltation traps described by Goossens et al. (2000), other saltation trap designs (e.g., Greeley et al., 1982; Nickling and McKenna Neuman, 1997; Ridge et al., 2011; Rotnicka, 2013; Sherman et al., 2014; Hilton et al., 2017) provide possible advantages in cost, portability, and consistency. Ideally, LF traps deployed in future studies would display consistent performance for all wind speeds and grain sizes. Without such reliability, the data are only internally relative and may be of limited utility outside of the individual study (Barchyn et al., 2011). To address potential inconsistencies among LF saltation trap measurements, further work should be undertaken to directly compare the performance of the many saltation traps that have proliferated over the past few years (e.g., Ridge et al., 2011; Rotnicka, 2013; Sherman et al., 2014; Hilton et al., 2017) and to better quantify the flux contributions of reptating and creeping particles very close (< 2 cm) to the sand surface (e.g., Swann and Sherman, 2013). These trap designs should be standardized such that any calibration work can be applied widely.

In addition to LF saltation trap consistency, the spatial footprint of LF traps is important. An issue with the BSNE traps used in our deployment is their large vertical range, which requires us to (1) estimate the representative height of each trap (Section 4.1) and (2) spatially separate the traps in the spanwise direction to provide higher resolution on the vertical profile (Section 2). Had we used traps with smaller cross-sectional areas, such as MWACs, we would have been able to achieve a closer vertical spacing of traps over a smaller areal footprint. Alternatively, deployment of traps covering the full vertical range of the saltation profile could eliminate the need to estimate the total flux from profile fitting. LF traps capable of providing both vertical profiles and direct total flux measurements include wedge traps (e.g., Greeley et al., 1982; Nickling and McKenna Neuman, 1997), mesh traps (Sherman et al., 2014; Hilton et al., 2017), and other custom-designed vertical traps (e.g., Rotnicka, 2013). However, such profiler traps capture smaller amounts of sand, requiring more frequent trap collection during strong saltation. More frequent LF measurements could improve the quality of HF sensor calibrations by accounting for rapid changes in wind direction (in the case of rotating traps like the BSNEs) or grain size; however, the smaller samples could also introduce sampling uncertainty in saltation flux calculations, especially during weak saltation. One additional strategy could be to separately measure total fluxes directly with trench traps (e.g., Greeley et al., 1996; Jackson, 1996), which could independently confirm the validity of total fluxes estimated from vertical profile fits.

5.2.2. High-frequency instrument selection

In addition to practical concerns (cost, instrument degradation, deployment scheme), there are two primary technical considerations when choosing HF saltation sensors: consistency and sensitivity. For consistency, we desire that the sensor efficiency (i.e., particle counts per flux) remains roughly constant regardless of saltation intensity; otherwise, the empirical calibration we describe here is not feasible (though more careful, lab-based calibration could still be possible). Sensit piezoelectric impact sensors appear to provide the most consistent saltation response for a variety of weather conditions (Hugenholtz and Barchyn, 2011), though they are also the costliest and most insensitive HF sensors (Stout and Zobeck, 1997). In contrast, Safire piezoelectric impact sensors, though capable of sampling at 20 Hz

Table 2
Instrumentation for field deployments to characterize high-frequency (HF) fluctuations of saltation mass flux.

Instrument type	Instrument options	Points to consider
Low-frequency (LF) saltation traps	BSNEs, MWACs, mesh traps, wedge traps, trench traps, automated traps, custom passive traps	Consistency of measurements, disruption of airflow, spatial footprint, vertical coverage, required collection interval
High-frequency (HF) saltation sensors	Optical sensors (Wenglor, Nikolich), piezoelectric impact sensors (Sensit, Safire), acoustic impact sensors (Saltiphone, Miniphone), other techniques (e.g., videography)	Consistency, sensitivity, sampling interval, reliability and drift of measurements
Distance sensors	Laser sensors (Sick), acoustic sensors (Senix)	Accuracy, sampling area
Dataloggers	Campbell Scientific, Hobo	Sufficient ports and processing speed for data streams, synchronization, ruggedness, sampling frequency

or higher frequencies, are subject to strong inconsistencies among instruments and over time (Baas, 2008). In particular, all circular piezoelectric sensors have an important momentum and sampling area bias that has relatively unquantified effects on the measurement efficacy (Barchyn and Hugenholtz, 2010). As for Saltiphone acoustic impact sensors, wind tunnel observations by Sterk et al. (1998) indicated consistent sensor mass flux responses in comparison to traps, whereas Goossens et al. (2000) showed that these sensors provide inconsistent results with changing wind speed, especially for coarser grain-size fractions. Wenglor optical counters appear to provide the most consistent particle counts over a reasonably wide range of saltation intensities (Hugenholtz and Barchyn, 2011), and, in contrast to past suggestion (e.g., Sherman et al., 2011), optical sensor saturation appears not to be a problem (Section 4.2). As we described above (Section 5.1), optical sensors show a degradation in consistency due to scratching or buildup of dust on the lenses (Barchyn et al., 2014a), but this can mostly be addressed through application of calibration techniques. In the future, new optical sensor technologies, such as the recently developed optical "Nikolich" sensors (Etyemezian et al., 2017), may overcome the need for calibration, by directly measuring and compensating for instrument drift, changes in ambient lighting, or variation in grain size (e.g., Barchyn et al., 2014a; Duarte-Campos et al., 2017).

For sensitivity, we recommend sensors that are capable of detecting small particles and subtle variations of saltation flux. Such information is useful, in particular, for understanding the highest-frequency component of the saltation signal. However, for the purposes of determining saltation flux by our calibration method, sensitivity is less essential than consistency, because differences in HF sensor sensitivities will simply be reflected in differences of their calibration factors. In general, acoustic sensors appear to be more sensitive than piezoelectric sensors (Sherman et al., 2011), which display a range of sensitivities (Barchyn and Hugenholtz, 2010). Optical sensors appear to provide intermediate sensitivity (Hugenholtz and Barchyn, 2011; Leonard et al., 2011), though Wenglor sensors appear unable to detect individual particles of $<200\ \mu m$ diameter (Duarte-Campos et al., 2017; Leonard et al., 2011). To overcome these issues of grain-size sensitivity bias, HF sensors should be developed in the future to directly detect airborne particle size distributions, such as through application of optical disdrometer techniques typically used for characterizing the size of rain droplets (e.g., Löffler-Mang and Joss, 2000).

5.2.3. Other measurements to include in saltation characterization deployments

In addition to LF and HF saltation measurements, we also included auxiliary measurements in our deployments to inform our calibration of HF saltation flux time series. At all of our field deployment sites, we mounted laser distance sensors with optical particle counters to detect variations of bed elevation (Section 3.2.3). Based on the known vertical displacement between distance sensors and saltation sensors, we could then calculate saltation sensor heights with respect to the bed surface (Supporting Information Section S1.7). In calculating saltation sensor heights, we did not consider high-frequency variations of bed elevation associated with the passage of ripples; instead, we considered the time-averaged bed elevation, representative of a spatial integration of upwind saltator sources. Distance sensors are thus useful primarily for detecting slower changes in the height of saltation sensors, such as those originating from settling of sensor towers or scour of the sand bed. We found the Sick DT35 laser distance sensors to provide relatively clean and accurate signals of bed elevation fluctuations (also useful for tracking ripple migration). In contrast, Senix acoustic distance sensors, tested at the Jericoacoara field site, provided much lower resolution and noisy bed elevation time series, due, in part, to the difficulty of electrically grounding these instruments in the dry, electrified environment of aeolian saltation.

Another essential instrument to include in a field deployment is a datalogger capable of recording the particle counts generated by HF sensors. We used Campbell CR1000 dataloggers, recording at 25 Hz, for this purpose. But other dataloggers, such as the Hobo (e.g., Davidson-Arnott et al., 2012), have also been commonly used in tandem with Wenglors and other saltation particle counters. When choosing dataloggers, it is important to ensure that they contain sufficient ports and processing speed to sustain the synchronous acquisition not just of HF saltation sensor data streams but also data streams from distance sensors, anemometers, and other instruments. To record the many instruments in our field deployments, we synchronized the data records from multiple Campbell CR1000 dataloggers. Higher quality dataloggers have better internal clocks, which facilitate better time sync between various loggers.

5.2.4. Protocols for instrument layout

One key assumption underlying our calibration protocols is the comparability of LF and HF saltation flux measurements. A key consideration in laying out instruments, therefore, is to ensure, as much as possible, that measurements from traps and sensors are temporally and spatially coincident. Temporal coincidence can be ensured for LF traps by coordinating trap collection times as closely as possible; for HF sensors, by properly synchronizing datalogger pulse counting. Such synchronization of manually-recorded LF trap time intervals with automated HF time-stamping is primarily a logistical issue, which requires that field workers take care in planning their deployment strategy.

For spatial coincidence, the characteristic spatial and temporal variability of saltation must be considered. Saltation varies spatially over spanwise distances greater than ~ 10 cm with the passage of streamers on ~ 1 s timescales (Baas and Sherman, 2005). Ideally, each HF sensor would be exactly co-located with a calibrating LF trap to reduce this variation, and all sensors and traps would be commonly aligned with respect to the wind (i.e., both fixed or both freely rotating). In practice, instruments may need to be spatially separated and differentially mounted to accommodate their size, reduce airflow interference among instruments, and fulfill other practical deployment needs. In our deployment, the somewhat bulky instruments (BSNEs as LF traps, Wenglors as HF sensors), necessitated some spatial separation, which thus required us to assume spatial homogeneity in long-term saltation fluxes. In addition, whereas our LF traps could freely rotate with the wind, our HF sensors required mounting in a rigid configuration, introducing possible additional uncertainty in our calibration method (Section 4.2.3). Nonetheless, our measurements show that spatially distributed instrument configurations, when necessary, can still provide reliable high-frequency saltation measurements.

In future deployments, selection of alternative LF traps and HF sensors could accommodate better collocation among instruments and consistency in mounting orientations (Section 5.2.1). By reducing the spatial footprint of the collection of measurements required to provide a single calibrated HF saltation flux time series, it would then be possible to more robustly measure spanwise or longitudinal patterns in the variation in turbulence-driven saltation flux variability, such as related to vegetation (e.g., Stockton and Gillette, 1990; Davidson-Arnott et al., 2012; Barrineau and Ellis, 2013; Chapman et al., 2013), soil moisture (e.g., Arens, 1996), dune topography (e.g., Bauer et al., 2012, 2015; Hoonhout and de Vries, 2017), or aeolian streamers (e.g., Baas and Sherman, 2005). However, the choice of any LF trap must be supported by evidence that absolute saltation flux measurements are reliable, and the selection of HF sensors must be supported by evidence of consistent performance for a wide range of saltation fluxes.

5.2.5. Selection of sampling time intervals

There are three time intervals associated with our method of characterizing high-frequency variation of saltation flux. First, there is the time interval for low-frequency (i.e., trap) measurements. This time interval should be long enough to ensure that all traps capture enough sand such that the errors associated with weighing the sand are small

relative to sand mass. However, LF measurement intervals must be short enough that such collections can keep pace with possible changes in the calibration of the high-frequency (HF) sensors (Section 4.2.3) or saltation profile shape (Bauer and Davidson-Arnott, 2014). Second, there is the sampling interval of HF sensors. This sampling interval will be determined, in part, by the technical capabilities of the saltation sensors and dataloggers used for the deployment. Ideally, the sampling interval will be as small as possible; but, in practice, the minimum sampling interval can be chosen according to the specific goals of the field deployment and the equipment available. Third, there is the subsampling interval Δt for characterization of the saltation flux for the high-frequency sensors. In principle, it is possible to reduce Δt to the sensor sampling interval; however, as we described in Section 4.3 above, fitting of saltation flux profiles becomes increasingly difficult for small Δt, especially when saltation is weak. Furthermore, if HF sensors are spatially separated, they may not provide comparable measures of saltation flux for $\Delta t < 0.1$ s due to the spatial variability of aeolian streamers.

5.2.6. The role of standardization

Differences in saltation measurement methods have inhibited inter-study comparisons of aeolian processes, leading for a call to adopt a common set of "standards" for the collection of aeolian field data (Barchyn et al., 2011). In response to this call, Webb et al. (2016b) have adopted a standard selection and configuration of instruments for their National Wind Erosion Research Network. Our methodology offers a complementary approach to inter-study comparisons that does not necessarily require such a standardized set of instruments. Instead, by providing a detailed set of protocols for combining LF trap and HF sensor data to characterize high-frequency variability in saltation flux driven by atmospheric turbulence, our methodology offers the possibility for future comparisons of data from across studies utilizing different combinations of instruments. Future work could evaluate the appropriateness of different traps and sensors in performing such inter-study comparisons, making measurements of aeolian saltation more useful and valuable.

5.3. Opportunities offered by high-frequency saltation datasets

Our calibrated HF field measurements of aeolian saltation offer unprecedented detail on saltation flux profiles and variability under a range of natural conditions. To our knowledge, the longest comparable field dataset was presented by Sherman et al. (1998). However, the duration of the Sherman et al. (1998) data set is only about 15 h, compared to the 75 h of active saltation that we measured, and the temporal resolution of their data (1 Hz) is substantially lower than ours (25 Hz). Baas and Sherman (2005) collected field data with comparable temporal resolution as ours, but their data span less than 1 h of active saltation. Our field data therefore offer substantial opportunities to understand various aspects of saltation process mechanics. These data have already been used to investigate the saltation flux law (Martin and Kok, 2017a) and saltation thresholds (Martin and Kok, 2017b). Further analyses could reveal how interactions between atmospheric turbulence and the saltation layer structure affect variability in saltation flux (e.g., Baas and Sherman, 2005), the saltation saturation time scale (Pähtz et al., 2013), and momentum transport in the saltation layer (Sherman and Farrell, 2008; Li et al., 2010). Because the dust emission flux is roughly proportional to the sand flux (Shao et al., 1993; Marticorena and Bergametti, 1995; Kok et al., 2014), these data also offer opportunities for the development of more accurate dust emission models.

6. Conclusion

In this paper, we presented a new methodology for characterizing high-frequency fluctuations of aeolian saltation flux. Our methodology combines low-frequency (LF) saltation traps that provide absolute saltation fluxes and high-frequency (HF) sensors that detect relative changes of saltation fluxes on short time scales. The increased accuracy of high-frequency saltation flux estimates facilitated by this new approach is a prerequisite for understanding how saltation responds to variations of wind and associated turbulence structures. As such, the measurements and analysis workflow presented here could play an important role in developing more accurate aeolian transport models that move beyond the common assumption of steady-state time-averaged saltation dynamics.

Acknowledgements

This work was supported by U.S. National Science Foundation (NSF) Postdoctoral Fellowship EAR-1249918 to R.L.M., NSF grant AGS-1358621 to J.F.K., Natural Sciences and Engineering Research Council of Canada (NSERC) support to C.H.H., NSF grant AGS-1358593 to M.C., and a Core Fulbright U.S. Scholar Program award to J.T.E. Research was also sponsored by the Army Research Laboratory and was accomplished under Grant Number W911NF-15-1-0417. The views and conclusions contained in this document are those of the authors and should not be interpreted as representing the official policies, either expressed or implied, of the Army Research Laboratory or the U.S. Government. The U.S. Government is authorized to reproduce and distribute reprints for Government purposes notwithstanding any copyright notation herein. Jericoacoara fieldwork is registered with the Brazilian Ministry of the Environment (#46254-1 to J.T.E.). Oceano Dunes State Vehicular Recreation Area, Rancho Guadalupe Dunes Preserve, and Jericoacoara National Park provided essential site access and support. We thank Doug Jerolmack for lab access for grain-size analysis, and Paulo Sousa, Peter Li, Francis Turney, Arkayan Samaddar, and Livia Freire for field assistance. Data and scripts associated with the methodology presented here may be accessed through the Mendeley data repository at https://doi.org/10.17632/mzm7r4hw7s.1.

Appendix A. Supporting information

Supporting information associated with this article can be found, in the online version, at http://dx.doi.org/10.1016/j.aeolia.2017.12.003.

References

Andreotti, B., 2004. A two-species model of aeolian sand transport. J. Fluid Mech. 510, 47–70. http://dx.doi.org/10.1017/S0022112004009073.

Arens, S.M., 1996. Rates of aeolian transport on a beach in a temperate humid climate. Geomorphology 17, 3–18. http://dx.doi.org/10.1016/0169-555X(95)00089-N.

Baas, A.C.W., 2008. Challenges in aeolian geomorphology: Investigating aeolian streamers. Geomorphology 93, 3–16. http://dx.doi.org/10.1016/j.geomorph.2006.12.015.

Baas, A.C.W., 2006. Wavelet power spectra of aeolian sand transport by boundary layer turbulence. Geophys. Res. Lett. 33, L05403. http://dx.doi.org/10.1029/2005GL025547.

Baas, A.C.W., 2004. Evaluation of saltation flux impact responders (Safires) for measuring instantaneous aeolian sand transport intensity. Geomorphology 59, 99–118. http://dx.doi.org/10.1016/j.geomorph.2003.09.009.

Baas, A.C.W., Sherman, D.J., 2005. Formation and behavior of aeolian streamers. J. Geophys. Res. 110, F03011. http://dx.doi.org/10.1029/2004JF000270.

Bagnold, R.A., 1941. The Physics of Blown Sand and Desert Dunes. Dover, London.

Barchyn, T.E., Hugenholtz, C.H., 2011. Comparison of four methods to calculate aeolian sediment transport threshold from field data: Implications for transport prediction and discussion of method evolution. Geomorphology 129, 190–203. http://dx.doi.org/10.1016/j.geomorph.2011.01.022.

Barchyn, T.E., Hugenholtz, C.H., 2010. Field comparison of four piezoelectric sensors for detecting aeolian sediment transport. Geomorphology 120, 368–371. http://dx.doi.org/10.1016/j.geomorph.2010.03.034.

Barchyn, T.E., Hugenholtz, C.H., Ellis, J.T., 2011. A call for standardization of aeolian process measurements: moving beyond relative case studies. Earth Surf. Process. Landf. 36, 702–705. http://dx.doi.org/10.1002/esp.2136.

Barchyn, T.E., Hugenholtz, C.H., Li, B., McKenna Neuman, C., Sanderson, R.S., 2014a. From particle counts to flux: Wind tunnel testing and calibration of the "Wenglor" aeolian sediment transport sensor. Aeolian Res. 15, 311–318. http://dx.doi.org/10.1016/j.aeolia.2014.06.009.

Barchyn, T.E., Martin, R.L., Kok, J.F., Hugenholtz, C.H., 2014b. Fundamental mismatches between measurements and models in aeolian sediment transport prediction: the role

of small-scale variability. Aeolian Res. 15, 245–251. http://dx.doi.org/10.1016/j.aeolia.2014.07.002.
Barrineau, C.P., Ellis, J.T., 2013. Sediment transport and wind flow around hummocks. Aeolian Res. 8, 19–27. http://dx.doi.org/10.1016/j.aeolia.2012.10.002.
Bauer, B.O., Davidson-Arnott, R.G.D., 2014. Aeolian particle flux profiles and transport unsteadiness. J. Geophys. Res. Earth Surf. 119, 1542–1563. http://dx.doi.org/10.1002/2014JF003128.
Bauer, B.O., Davidson-Arnott, R.G.D., Walker, I.J., Hesp, P.A., Ollerhead, J., 2012. Wind direction and complex sediment transport response across a beach-dune system. Earth Surf. Process. Landf. 37, 1661–1677. http://dx.doi.org/10.1002/esp.3306.
Bauer, B.O., Hesp, P.A., Walker, I.J., Davidson-Arnott, R.G.D., 2015. Sediment transport (dis)continuity across a beach–dune profile during an offshore wind event. Geomorphology 245, 135–148. http://dx.doi.org/10.1016/j.geomorph.2015.05.004.
Bauer, B.O., Namikas, S.L., 1998. Design and field test of a continuously weighing, tipping-bucket assembly for aeolian sand traps. Earth Surf. Process. Landf. 23, 1171–1183. http://dx.doi.org/10.1002/(SICI)1096-9837(199812)23:13<1171::AID-ESP925>3.0.CO;2-H.
Bellot, H., Bouvet, F.N., Piard, L., Palerme, C., Genthon, C., 2013. Drifting and blowing snow measurements: comparison between Snow Particle counter and a simple photoelectronic fork sensor (Wenglor). In: Presented at the International Snow Science Workshop (ISSW), Irstea, ANENA, Meteo France, pp. 1009–1013.
Bridges, N.T., Ayoub, F., Avouac, J.-P., Leprince, S., Lucas, A., Mattson, S., 2012. Earth-like sand fluxes on Mars. Nature 485, 339–342. http://dx.doi.org/10.1038/nature11022.
Butterfield, G.R., 1991. Grain transport rates in steady and unsteady turbulent airflows. Acta Mech. Suppl 1, 97–122.
Carneiro, M.V., Araújo, N.A.M., Pähtz, T., Herrmann, H.J., 2013. Midair collisions enhance saltation. Phys. Rev. Lett. 111, 58001. http://dx.doi.org/10.1103/PhysRevLett. 111.058001.
Chapman, C., Walker, I.J., Hesp, P.A., Bauer, B.O., Davidson-Arnott, R.G.D., Ollerhead, J., 2013. Reynolds stress and sand transport over a vegetated foredune. Earth Surf. Process. Landf. 38, 1623–1764. http://dx.doi.org/10.1002/esp.3428.
Chepil, W.S., 1945. Dynamics of Wind Erosion. 1. Nature of movement of soil by wind. Soil Sci. 60, 305–320. http://dx.doi.org/10.1097/00010694-194510000-00004.
Cooper, W.S., 1967. Coastal Dunes of California. Geological Society of America Memoir 104.
Davidson-Arnott, R.G.D., Bauer, B.O., Walker, I.J., Hesp, P.A., Ollerhead, J., Chapman, C., 2012. High-frequency sediment transport responses on a vegetated foredune. Earth Surf. Process. Landf. 37, 1227–1241. http://dx.doi.org/10.1002/esp.3275.
Davidson-Arnott, R.G.D., Bauer, B.O., Walker, I.J., Hesp, P.A., Ollerhead, J., Delgado-Fernandez, I., 2009. Instantaneous and mean aeolian sediment transport rate on beaches: an intercomparison of measurements from two sensor types. J. Coast. Res. 1, 297–301.
Davidson-Arnott, R.G.D., Yang, Y., Ollerhead, J., Hesp, P.A., Walker, I.J., 2008. The effects of surface moisture on aeolian sediment transport threshold and mass flux on a beach. Earth Surf. Process. Landf. 33, 55–74. http://dx.doi.org/10.1002/esp.1527.
Delgado-Fernandez, I., Davidson-Arnott, R., Bauer, B.O., Walker, I.J., Ollerhead, J., Rhew, H., 2012. Assessing aeolian beach-surface dynamics using a remote sensing approach. Earth Surf. Process. Landf. 37, 1651–1660. http://dx.doi.org/10.1002/esp.3301.
Dong, Z., Lu, J., Man, D., Lv, P., Qian, G., Zhang, Z., Luo, W., 2011. Equations for the near-surface mass flux density profile of wind-blown sediments. Earth Surf. Process. Landf. 36, 1292–1299. http://dx.doi.org/10.1002/esp.2151.
Dong, Z., Lv, P., Zhang, Z., Qian, G., Luo, W., 2012. Aeolian transport in the field: a comparison of the effects of different surface treatments. J. Geophys. Res. 117, D09210. http://dx.doi.org/10.1029/2012JD017538.
Duarte-Campos, L., Wijnberg, K.M., Oyarte-Gálvez, L., Hulscher, S.J.M.H., 2017. Laser particle counter validation for aeolian sand transport measurements using a high-speed camera. Aeolian Res. 25, 37–44. http://dx.doi.org/10.1016/j.aeolia.2017.02.002.
Dupont, S., Bergametti, G., Marticorena, B., Simoëns, S., 2013. Modeling saltation intermittency. J. Geophys. Res. Atmos. 118, 7109–7128. http://dx.doi.org/10.1002/jgrd.50528.
Durán, O., Claudin, P., Andreotti, B., 2011. On aeolian transport: Grain-scale interactions, dynamical mechanisms and scaling laws. Aeolian Res. 3, 243–270. http://dx.doi.org/10.1016/j.aeolia.2011.07.006.
Durán, O., Moore, L.J., 2013. Vegetation controls on the maximum size of coastal dunes. Proc. Natl. Acad. Sci. U.S.A. 110, 17217–17222. http://dx.doi.org/10.1073/pnas.1307580110.
Ellis, J.T., Li, B., Farrell, E.J., Sherman, D.J., 2009a. Protocols for characterizing aeolian mass-flux profiles. Aeolian Res. 1, 19–26. http://dx.doi.org/10.1016/j.aeolia.2009.02.001.
Ellis, J.T., Morrison, R.F., Priest, B.H., 2009b. Detecting impacts of sand grains with a microphone system in field conditions. Geomorphology 105, 87–94. http://dx.doi.org/10.1016/j.geomorph.2008.02.017.
Etyemezian, V., Nikolich, G., Nickling, W., King, J.S., Gillies, J.A., 2017. Analysis of an optical gate device for measuring aeolian sand movement. Aeolian Res. 24, 65–79. http://dx.doi.org/10.1016/j.aeolia.2016.11.005.
Farrell, E.J., Sherman, D.J., Ellis, J.T., Li, B., 2012. Vertical distribution of grain size for wind blown sand. Aeolian Res. 7, 51–61. http://dx.doi.org/10.1016/j.aeolia.2012.03.003.
Fryrear, D.W., 1986. A field dust sampler. J. Soil Water Conserv. 41, 117–120.
Fryrear, D.W., Saleh, A., 1993. Field wind erosion: vertical distribution. Soil Sci. 155, 294–300. http://dx.doi.org/10.1097/00010694-199304000-00008.
Gillette, D.A., Adams, J.A., Muhs, D., Kihl, R., 1982. Threshold friction velocities and rupture moduli for crusted desert soils for the input of soil particles into the air. J. Geophys. Res. 87, 9003–9015.
Gillette, D.A., Blifford, I.H., Fryrear, D.W., 1974. The influence of wind velocity on the size distributions of aerosols generated by the wind erosion of soils. J. Geophys. Res. 79, 4068–4075. http://dx.doi.org/10.1029/JC079i027p04068.
Goossens, D., Offer, Z., London, G., 2000. Wind tunnel and field calibration of five aeolian sand traps. Geomorphology 35, 233–252. http://dx.doi.org/10.1016/S0169-555X(00)00041-6.
Greeley, R., Blumberg, D.G., Williams, S.H., 1996. Field measurements of the flux and speed of wind-blown sand. Sedimentology 43, 41–52. http://dx.doi.org/10.1111/j.1365-3091.1996.tb01458.x.
Greeley, R., Leach, R.N., Williams, S.H., White, B.R., Pollack, J.B., Krinsley, D.H., Marshall, J.R., 1982. Rate of wind abrasion on Mars. J. Geophys. Res. Solid Earth 87, 10009–10024. http://dx.doi.org/10.1029/JB087iB12p10009.
Haustein, K., Washington, R., King, J., Wiggs, G., Thomas, D.S.G., Eckardt, F.D., Bryant, R.G., Menut, L., 2015. Testing the performance of state-of-the-art dust emission schemes using DO4Models field data. Geosci. Model. Dev. 8, 341–362. http://dx.doi.org/10.5194/gmd-8-341-2015.
Hilton, M., Nickling, B., Wakes, S., Sherman, D., Konlechner, T., Jermy, M., Geoghegan, P., 2017. An efficient, self-orienting, vertical-array, sand trap. Aeolian Res. 25, 11–21. http://dx.doi.org/10.1016/j.aeolia.2017.01.003.
Hoonhout, B., de Vries, S., 2017. Field measurements on spatial variations in aeolian sediment availability at the Sand Motor mega nourishment. Aeolian Res. 24, 93–104. http://dx.doi.org/10.1016/j.aeolia.2016.12.003.
Hugenholtz, C.H., Barchyn, T.E., 2011. Laboratory and field performance of a laser particle counter for measuring aeolian sand transport. J. Geophys. Res. 116, F01010. http://dx.doi.org/10.1029/2010JF001822.
Iversen, J.D., Rasmussen, K.R., 1999. The effect of wind speed and bed slope on sand transport. Sedimentology 46, 723–731. http://dx.doi.org/10.1046/j.1365-3091.1999.00245.x.
Jackson, D.W.T., 1996. Potential inertial effects in aeolian sand transport: preliminary results. Sediment. Geol. 106, 193–201. http://dx.doi.org/10.1016/S0037-0738(96)00002-4.
Jerolmack, D.J., Reitz, M.D., Martin, R.L., 2011. Sorting out abrasion in a gypsum dune field. J. Geophys. Res. Earth Surf. 116, F02003. http://dx.doi.org/10.1029/2010JF001821.
Kok, J.F., Mahowald, N.M., Fratini, G., Gillies, J.A., Ishizuka, M., Leys, J.F., Mikami, M., Park, M.-S., Park, S.-U., Van Pelt, R.S., Zobeck, T.M., 2014. An improved dust emission model – part 1: model description and comparison against measurements. Atmos. Chem. Phys. 14, 13023–13041. http://dx.doi.org/10.5194/acp-14-13023-2014.
Kok, J.F., Parteli, E.J.R., Michaels, T.I., Karam, D.B., 2012. The physics of wind-blown sand and dust. Rep. Prog. Phys. 75, 106901. http://dx.doi.org/10.1088/0034-4885/75/10/106901.
Kok, J.F., Renno, N.O., 2008. Electrostatics in wind-blown sand. Phys. Rev. Lett. 100, 14501. http://dx.doi.org/10.1103/PhysRevLett. 100.014501.
Lancaster, N., 1988. Controls of eolian dune size and spacing. Geology 16, 972–975.
Leonard, K.C., Tremblay, L.-B., Thom, J.E., MacAyeal, D.R., 2011. Drifting snow threshold measurements near McMurdo station, Antarctica: a sensor comparison study. Cold Reg. Sci. Technol. 70, 71–80. http://dx.doi.org/10.1016/j.coldregions.2011.08.001.
Li, B., McKenna Neuman, C., 2014. A wind tunnel study of aeolian sediment transport response to unsteady winds. Geomorphology 214, 261–269. http://dx.doi.org/10.1016/j.geomorph.2014.02.010.
Li, B., McKenna Neuman, C., 2012. Boundary-layer turbulence characteristics during aeolian saltation. Geophys. Res. Lett. 39, L11402. http://dx.doi.org/10.1029/2012GL052234.
Li, B., Sherman, D.J., Farrell, E.J., Ellis, J.T., 2010. Variability of the apparent von Karman parameter during aeolian saltation. Geophys. Res. Lett. 37, L15404. http://dx.doi.org/10.1029/2010GL044068.
Löffler-Mang, M., Joss, J., 2000. An optical disdrometer for measuring size and velocity of hydrometeors. J. Atmospheric Ocean. Technol. 17, 130–139. http://dx.doi.org/10.1175/1520-0426(2000) 017<0130:AODFMS>2.0.CO;2.
Maggioni, M., Durand, N., Frigo, B., Pallara, O., Freppaz, M., Dellavedova, P., Segor, V., Naaim Bouvet, F., Bellot, H., 2013. Preliminary measurements and survey of snow-drift at the seehore avalanche test site – Aosta Valley (IT). In: International Snow Science Workshop (ISSW). Irstea, ANENA, Meteo France, Grenoble – Chamonix Mont-Blanc, France, pp. 126–133.
Marticorena, B., Bergametti, G., 1995. Modeling the atmospheric dust cycle: 1. Design of a soil-derived dust emission scheme. J. Geophys. Res. Atmospheres 100, 16415–16430. http://dx.doi.org/10.1029/95JD00690.
Martin, R.L., Barchyn, T.E., Hugenholtz, C.H., Jerolmack, D.J., 2013. Timescale dependence of aeolian sand flux observations under atmospheric turbulence. J. Geophys. Res. Atmos. 118, 9078–9092. http://dx.doi.org/10.1002/jgrd.50687.
Martin, R.L., Kok, J.F., 2017a. Wind-invariant saltation heights imply linear scaling of aeolian saltation flux with shear stress. Sci. Adv. 3. http://dx.doi.org/10.1126/sciadv.1602569.
Martin, R.L., Kok, J.F., 2017b. Field measurements demonstrate distinct initiation and cessation thresholds governing aeolian sediment transport flux. arXiv:1610.10059v5 [physics.geo-ph].
Massey, J., 2013. A Wind Tunnel Investigation to Examine the Role of Air Humidity in Controlling the Threshold Shear Velocity of a Surface and in Controlling the Mass Flux of Material from a Surface (Thesis). Texas Tech University, Lubbock, TX.
McKenna Neuman, C., Lancaster, N., Nickling, W.G., 2000. The effect of unsteady winds on sediment transport on the stoss slope of a transverse dune, Silver Peak, NV, USA. Sedimentology 47, 211. http://dx.doi.org/10.1046/j.1365-3091.2000.00289.x.
Namikas, S.L., 2003. Field measurement and numerical modelling of aeolian mass flux distributions on a sandy beach. Sedimentology 50, 303–326. http://dx.doi.org/10.1046/j.1365-3091.2003.00556.x.

Namikas, S.L., 2002. Field evaluation of two traps for high-resolution aeolian transport measurements. J. Coast. Res. 18, 136–148.
Nickling, W.G., McKenna Neuman, C., 1997. Wind tunnel evaluation of a wedge-shaped aeolian sediment trap. Geomorphology 18, 333–345. http://dx.doi.org/10.1016/S0169-555X(96)00040-2.
Nield, J.M., Wiggs, G.F.S., Baddock, M.C., Hipondoka, M.H.T., 2017. Coupling leeside grainfall to avalanche characteristics in aeolian dune dynamics. Geology 45, 271–274. http://dx.doi.org/10.1130/G38800.1.
Owen, P.R., 1964. Saltation of uniform grains in air. J. Fluid Mech. 20, 225–242. http://dx.doi.org/10.1017/S0022112064001173.
Pähtz, T., Kok, J.F., Parteli, E.J.R., Herrmann, H.J., 2013. Flux saturation length of sediment transport. Phys. Rev. Lett. 111, 218002.
Perkins, J.P., Finnegan, N.J., de Silva, S.L., 2015. Amplification of bedrock canyon incision by wind. Nat. Geosci. 8, 305–310. http://dx.doi.org/10.1038/ngeo2381.
Poortinga, A., Keijsers, J.G.S., Visser, S.M., Riksen, M.J.P.M., Baas, A.C.W., 2015. Temporal and spatial variability in event scale aeolian transport on Ameland, The Netherlands. GeoResJ 5, 23–35. http://dx.doi.org/10.1016/j.grj.2014.11.003.
Ridge, J.T., Rodriguez, A.B., Fegley, S.R., Browne, R., Hood, D., 2011. A new “pressure sensitive” method of measuring aeolian sediment transport using a Gauged Sediment Trap (GaST). Geomorphology 134, 426–430. http://dx.doi.org/10.1016/j.geomorph.2011.07.017.
Rotnicka, J., 2013. Aeolian vertical mass flux profiles above dry and moist sandy beach surfaces. Geomorphology 187, 27–37. http://dx.doi.org/10.1016/j.geomorph.2012.12.032.
Schönfeldt, H.J., 2004. Establishing the threshold for intermittent aeolian sediment transport. Meteorol. Z. 13, 437–444. http://dx.doi.org/10.1127/0941-2948/2004/0013-0437.
Schonfeldt, H.-J., von Lowis, S., 2003. Turbulence-driven saltation in the atmospheric surface layer. Meteorol. Z. 12, 257–268. http://dx.doi.org/10.1127/0941-2948/2003/0012-0257.
Shao, Y., Raupach, M.R., Findlater, P.A., 1993. Effect of saltation bombardment on the entrainment of dust by wind. J. Geophys. Res. 98, 12719–12726. http://dx.doi.org/10.1029/93JD00396.
Sherman, D.J., Farrell, E.J., 2008. Aerodynamic roughness lengths over movable beds: comparison of wind tunnel and field data. J. Geophys. Res. 113, F02S08. http://dx.doi.org/10.1029/2007JF000784.
Sherman, D.J., Jackson, D.W.T., Namikas, S.L., Wang, J., 1998. Wind-blown sand on beaches: an evaluation of models. Geomorphology 22, 113–133. http://dx.doi.org/10.1016/S0169-555X(97)00062-7.
Sherman, D.J., Li, B., 2012. Predicting aeolian sand transport rates: a reevaluation of models. Aeolian Res. 3, 371–378. http://dx.doi.org/10.1016/j.aeolia.2011.06.002.
Sherman, D.J., Li, B., Ellis, J.T., Farrell, E.J., Maia, L.P., Granja, H., 2013. Recalibrating aeolian sand transport models. Earth Surf. Process. Landf. 38, 169–178. http://dx.doi.org/10.1002/esp.3310.
Sherman, D.J., Li, B., Farrell, E.J., Ellis, J.T., Cox, W.D., Maia, L.P., Sousa, P.H.G.O., 2011. Measuring aeolian saltation: a comparison of sensors. J. Coast. Res. 59, 280–290. http://dx.doi.org/10.2112/SI59-030.1.
Sherman, D.J., Swann, C., Barron, J.D., 2014. A high-efficiency, low-cost aeolian sand trap. Aeolian Res. 13, 31–34. http://dx.doi.org/10.1016/j.aeolia.2014.02.006.
Sørensen, M., McEwan, I., 1996. On the effect of mid-air collisions on aeolian saltation. Sedimentology 43, 65–76. http://dx.doi.org/10.1111/j.1365-3091.1996.tb01460.x.
Spaan, W.P., van den Abeele, G.D., 1991. Wind borne particle measurements with acoustic sensors. Soil Technol. 4, 51–63. http://dx.doi.org/10.1016/0933-3630(91)90039-P.
Sterk, G., Jacobs, A.F.G., Van Boxel, J.H., 1998. The effect of turbulent flow structures on saltation sand transport in the atmospheric boundary layer. Earth Surf. Process. Landf. 23, 877–887.
Stockton, P.H., Gillette, D.A., 1990. Field measurement of the sheltering effect of vegetation on erodible land surfaces. Land Degrad. Dev. 2, 77–85. http://dx.doi.org/10.1002/ldr.3400020202.
Stout, J.E., Zobeck, T.M., 1997. Intermittent saltation. Sedimentology 44, 959–970. http://dx.doi.org/10.1046/j.1365-3091.1997.d01-55.x.
Swann, C., Sherman, D.J., 2013. A bedload trap for aeolian sand transport. Aeolian Res. 11, 61–66. http://dx.doi.org/10.1016/j.aeolia.2013.09.003.
Trujillo, E., Leonard, K., Maksym, T., Lehning, M., 2016. Changes in snow distribution and surface topography following a snowstorm on Antarctic sea ice. J. Geophys. Res. – Earth Surf. 121, 2172–2191.
Ungar, J.E., Haff, P.K., 1987. Steady state saltation in air. Sedimentology 34, 289–299. http://dx.doi.org/10.1111/j.1365-3091.1987.tb00778.x.
Weaver, C.M., Wiggs, G.F.S., 2011. Field measurements of mean and turbulent airflow over a barchan sand dune. Geomorphology 128, 32–41. http://dx.doi.org/10.1016/j.geomorph.2010.12.020.
Webb, N.P., Galloza, M.S., Zobeck, T.M., Herrick, J.E., 2016a. Threshold wind velocity dynamics as a driver of aeolian sediment mass flux. Aeolian Res. 20, 45–58.
Webb, N.P., Herrick, J.E., Van Zee, J.W., Courtright, E.M., Hugenholtz, C.H., Zobeck, T.M., Okin, G.S., Barchyn, T.E., Billings, B.J., Boyd, R., Clingan, S.D., Cooper, B.F., Duniway, M.C., Derner, J.D., Fox, F.A., Havstad, K.M., Heilman, P., LaPlante, V., Ludwig, N.A., Metz, L.J., Nearing, M.A., Norfleet, M.L., Pierson, F.B., Sanderson, M.A., Sharratt, B.S., Steiner, J.L., Tatarko, J., Tedela, N.H., Toledo, D., Unnasch, R.S., Van Pelt, R.S., Wagner, L., 2016b. The National Wind Erosion Research Network: building a standardized long-term data resource for aeolian research, modeling and land management. Aeolian Res. 22, 23–36. http://dx.doi.org/10.1016/j.aeolia.2016.05.005.
Wiggs, G.F.S., Atherton, R.J., Baird, A.J., 2004a. Thresholds of aeolian sand transport: establishing suitable values. Sedimentology 51, 95–108. http://dx.doi.org/10.1046/j.1365-3091.2003.00613.x.
Wiggs, G.F.S., Baird, A.J., Atherton, R.J., 2004b. The dynamic effects of moisture on the entrainment and transport of sand by wind. Geomorphology 59, 13–30. http://dx.doi.org/10.1016/j.geomorph.2003.09.002.
Zobeck, T.M., Fryrear, D.W., 1986. Chemical and physical characteristics of windblown sediment. Trans. Am. Soc. Agric. Eng. 29, 1032–1036.
Zobeck, T.M., Sterk, G., Funk, R., Rajot, J.L., Stout, J.E., Van Pelt, R.S., 2003. Measurement and data analysis methods for field-scale wind erosion studies and model validation. Earth Surf. Process. Landf. 28, 1163–1188.